Performance and Design Improvements Toward the Commercialization of a Needle-Free Jet Injector

by

Ashin Modak

Submitted to the Department of Mechanical Engineering
in partial fulfillment of the requirements for the degree of

Master of Science in Mechanical Engineering

at the

MASSACHUSETTS INSTITUTE OF TECHNOLOGY

June 2013

Author .....
Department of Mechanical Engineering
May 16, 2013

Certified by .....
Ian W. Hunter
Hatsopoulos Professor of Mechanical Engineering
Thesis Supervisor

Accepted by .....
David E. Hardt
Chairman, Department Committee on Graduate Students

Performance and Design Improvements Toward the Commercialization of a Needle-Free Jet Injector

by

Ashin Modak

Submitted to the Department of Mechanical Engineering
on May 16, 2013, in partial fulfillment of the
requirements for the degree of
Master of Science in Mechanical Engineering

Abstract

In the past years, the BioInstrumentation Lab has developed a handheld needle-free jet injector based on a custom Lorentz-force motor. While the current handheld design is effective as a research tool, many improvements are needed before it can be a commercially viable product for individual human use. Improvements in various aspects of the design have been implemented. A Hall effect sensor and a thermopile were added to provide critical safety and quality monitoring of the Lorentz-force motor, and a linear encoder provided increased position resolution. Flexible coil elements reduced drag on the coil while eliminating a mechanical failure mode caused by moving cables. A low cost optical encoder system has been implemented to provide 5 µm position resolution for the actuator and this has improved error of volume ejections to 0.3 µL. All these improvements have also been proved to be scalable by their implementation on a scaled down design of the current actuator. This actuator was modeled and verified to have approximatley half the force output of the current actuator, and is small and light enough to be packaged in a portable device. Lastly, an adaptor that allows extraction of drug out of a vial using the BioInstrumentation Lab's needle-free injector has been developed as well as an automatic detection scheme that expels any air drawn in by this extraction process with minimal fluid loss.

Thesis Supervisor: Ian W. Hunter
Title: Hatsopoulos Professor of Mechanical Engineering

Acknowledgments

I would like to first thank my family, who have constantly showered me with love over my 23 years. How they deal with such an ungrateful, good-for-nothing son and brother such as myself is beyond me, but I appreciate their efforts. To my parents, Pramod and Winaya Modak, thanks for taking such an interest in my life. I love how our relationship has changed over the years: I consider you two my oldest friends. As for my sister, Nina Sarika Modak, you are my favorite. I could go on and on about how much you inspire me, but I'm afraid it'll go to your head. If it were in fashion to dedicate a master's thesis, I would dedicate this to you, but alas, this is not the case.

Thanks to all of my friends. To everyone back home, I miss you terribly. Knowing that you all are rooting for me gives me the energy to put forth my best effort. To all my friends in Boston, thanks for enduring the complaining, yelling, nose-flicks, and general injuries that come with being my friend. You all keep me happy.

Thanks to all the mentors in my life: Sam Christensen, Alex Isbell, Jim Adam, and Jim Birdsong. Some of you I have thanked properly, some I haven't. Your influences in my adolescence shaped my values to what they are today. Thanks to Dr. Jenni Buckley and the rest of my colleagues at the Biomechancial Testing Facility. I realize now how special our time together was. Working with you all shook me out of my general undergraduate apathy and gave my education a direction and motivation. I hope one day I will be able to impact someone as positively as you all have with me.

Lastly, thanks to Professor Ian Hunter for both the opportunities and education that he and the rest of the BioInstrumentation Lab has provided. I came into this lab knowing very little about anything, especially mechanical engineering. Thanks to Adam Wahab, Dr. Brian Hemond, Dr. Bryan Ruddy, Dr. Cathy Hogan, Eli Paster, Ellen Chen, James White, Jean Chang, and John Liu for mentoring and bringing me up to speed. Thanks to Alison Cloutier, who I got to work with for the first six months in creating the improved benchtop injector, for dealing with the brunt of my general nonsense for two years.

Contents

List of Figures

List of Tables

Chapter 1

Background

1.1 History of Needle-Free Injection

Needle-free jet injection has been developed since the 1930's [1], and it was widely used by the US military in the 1970's as a means of vaccination. While these initial multi-use nozzle jet injectors (MUNJIs) devices proved successful in eradicating diseases such as smallpox [2], they were for the most part discontinued due to subject contamination. Since then various single-use, disposable cartridge jet injection devices (DCJIs) using compressed gas [3] [4], springs [5] [6] [7], or even explosive reactions [8] [9] have come onto the market for a variety of applications, including treatments for diabetes [10], growth hormone deficiencies [11], anesthetics [12], and DNA based therapies [13]. In particular, needle-free jet injection technology is of interest in insulin delivery because jet injectors are thought to be easier to use for those with impaired motor skills, a common deficiency in those with type II diabetes, and studies have shown that insulin delivery via jet injection more rapidly increased plasma insulin levels [2]. However, even these disposable cartridge jet injectors have not been universally adopted due to various complications such as "wet" injections in which fluid does not penetrate the skin, or excessive pain and bruising in certain injection types in which the fluid jet pierces further than intended into the body.

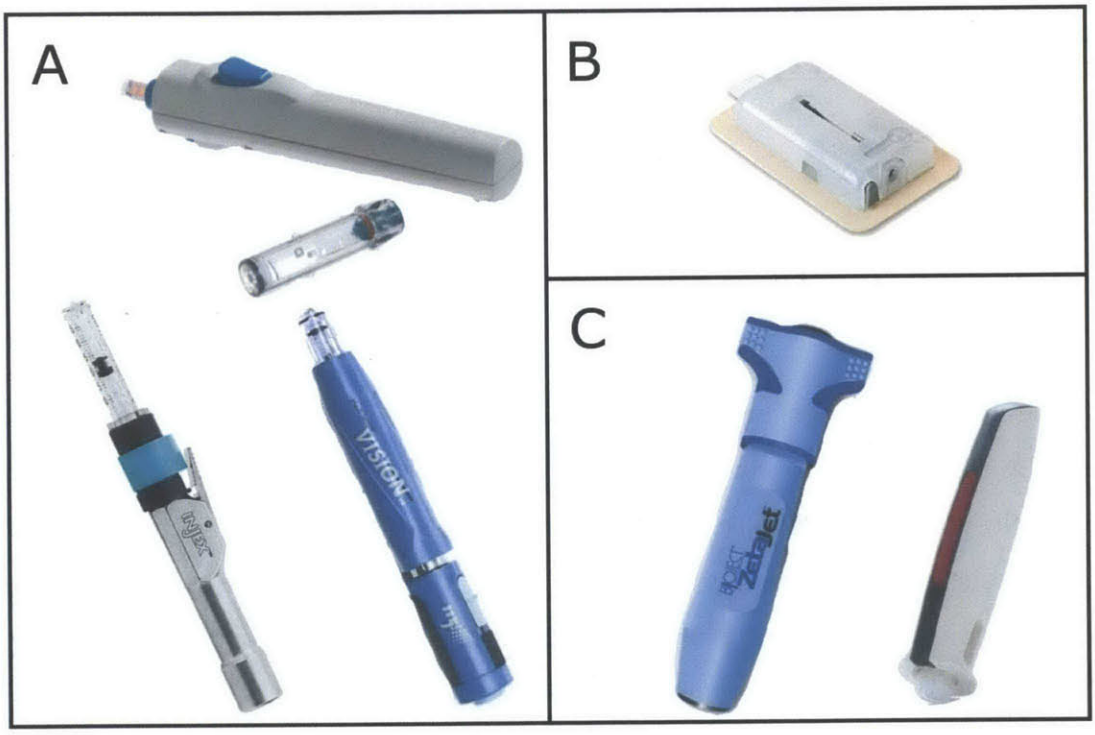

Figure 1-1: Various single-use needle-free injectors currently on the market. (A) Injectors that are driven by springs [5] [6] [7]. (B) Injectors driven by explosive reactions [9]. (C) Injectors driven by compressed gas [3] [4].

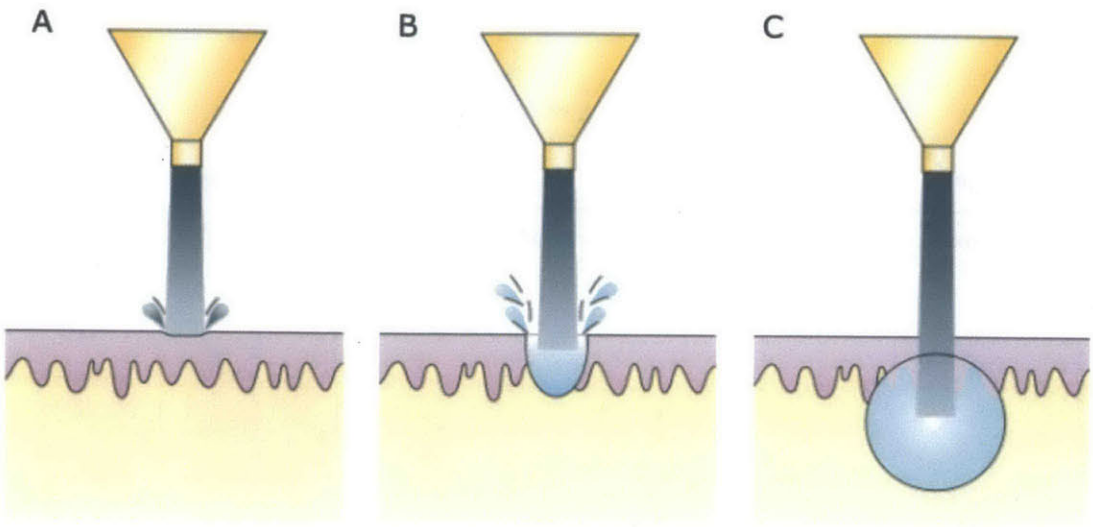

Figure 1-2: A model of the mechanics occurring during the jet injection process. (A) An initial high speed jet is used to break the skin, and (B) the depth of the opening created is dependent both on the speed and time of this initial piercing jet. (C) After the desired opening is created, jet velocity can be lowered as liquid is delivered to the desired depth and creates a bolus. Figure adapted from [2].

1.2 Mechanics of an Injection

To reduce the probability of these failure modes, it is important to understand the mechanics that occur during a jet injection. Work has been done both in the BioInstrumentation Lab [14] [15] [16] [17] [18] and elsewhere [2] [19] to determine the parameters critical to jet injection. The schematic of a jet injection is shown in Fig. 1-2: as the fluid jet rushes out of the nozzle at high velocity, it first pierces the skin, forming a hole via various skin failure modes including erosion and fracture. In particular, it has been found that injection depth and quality of injection can be controlled by both time of injection (t_{jet}) and initial jet speed (v_{jet}) [14] [16] [18] [19] [20]. Once this initial hole has been created, the fluid creates a bolus at this particular depth. If the needle-free injector is conrollable during the injection, this following velocity (v_{follow}) of the fluid jet can be decreased, only needing to be large enough to prevent resealing of the initial puncture during delivery.

It has been hypothesized that an incorrect penetration depth for shallow injections

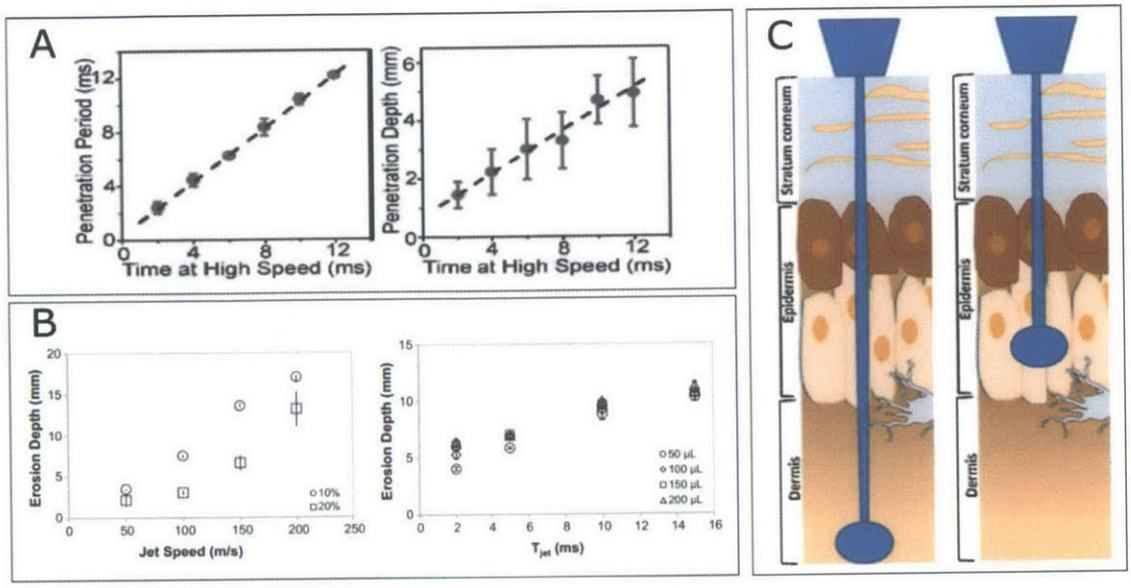

Figure 1-3: Studies both by others (A) [20] and our lab (B) [15] have shown that the depth at which drug is delivered can be controlled via the initial jet speed and time at which this initial jet is held at high speed. (C) This control of depth allows for delivery to various tissue layers. Images adapted from [15], [20], and [21]

is one cause for pain and bleeding [2]. Depending on the type of injection needed (epidermal, transcutaneous, intradermal, intramuscular or subcutaneous) injections may need to be delivered to various tissue layers of the body (see reffig:jet injection layers). While an injector may be calibrated for a certain type of injection, variability in skin dynamics can greatly affect the success of an injection [2] [21]. Many of the current injectors on the market, primarily spring powered ones, do not have the force range or velocity control to be versatile enough for this variability [21]. While others in academia have developed piezoelectric stack controlled injectors [20], they lack the range to truly be scalable for a wide variety of injection doses.

1.3 Lorentz-Force Actuators for Jet Injection

Much work has been done in the BioInstrumentation Lab in the development of a needle-free jet injector based on a Lorentz-force actuator. Both an auto-loading, benchtop device and a handheld device have been constructed and used to characterize jet injections. [14] [22] [23]. The efficacy of the handheld device has been shown in

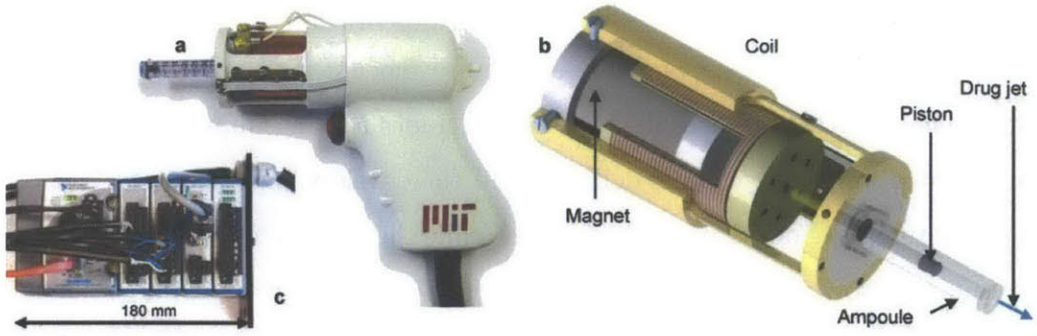

Figure 1-4: Various aspects of a portable jet injector system. (A) portable plastic housing (B) cutaway of actual device (C) compact RIO system used for control. Image reproduced from [15].

injections into acrylamide, various post mortem mammalian tissue, and live animals [14] [15] [16] [17]. This Lorentz-force actuated injector proved robust enough to be calibrated for a variety of different tissue types. In the development of this handheld device, a custom Lorentz-force actuator [23] needed to be designed, as outlined by [14]. This actuator is described further in later sections.

The entire system is currently being controlled in real time using a National Instruments Compact RIO Real Time Controller [24] as described in Taberner et al 2012 [15]. The majority of the control is run on a Xilinx FPGA at 100 kHz. Position feedback is provided via a linear pontentiometer [25]. All parts of the motor were fabricated in-house on a Mazak Turning Center [26].

1.4 Aims of this Thesis

While the current handheld design is effective for research, it is in its current state not viable as a commercial product for individual human use. More sensing must be integrated into the design to allow for monitoring of the motor and preventing device malfuction. It also would be ideal if the motor could be scaled down to allow for the device to be more portable. Finer control over the volume of fluid delivered would open more potential applications for the use of the injector. Lastly, the accessories a consumer would need to actually use this device, such as an adaptor between the

injector and a drug vial, need to be developed.

The goal of this thesis was to make improvements for commercialization of the existing needle-free injection device. This includes sensing improvements, scaling of the actuator, precision volume delivery, and the development of an interface to allow for extracting drug out of medicinal vials. While these challenges are not the only ones that must be solved to make the current needle-free jet injector commercializable for individual use, they are significant problems that must be addressed. The motivation for each undertaking is further provided in the subsequent chapters

Chapter 2

Hardware Modifications to the Current Jet Injector

2.1 Motivation for Hardware Improvements

One obstacle toward the commercialization of the Lorentz-force needle-free injector is the current design of the prototype. The current handheld design is too bulky, as the motor it uses has a diameter of 40 mm and has a mass of 500 g. The size of the motor made packaging it into a handheld device extremely difficult. Additionally, several sensing issues had to be addressed. Position readings of the jet injector coil needed to be improved to allow for more precise deliveries of smaller doses of drug. Finally, any packaged device would also need safety and quality checks to make sure that the motor stator has not demagnetized, or that the device has not overheated. In a commercial device, these checks must be done on board by the device itself instead of having to be diagnosed by the user. To this end, a new benchtop setup has been designed to solve these sensing concerns, and a smaller, more portable, motor has been designed that also takes advantage of these new sensing solutions.

2.2 State of the Art

As metioned earlier, the portable jet injector developed in the BioInstrumentation Lab uses a custom-made Lorentz-force actuator. The basic design was designed in the BioInstrumentation Lab [14] [23], and is shown in Fig. 2-1.

A single N50 neodymium rare earth magnet is surrounded by a low carbon steel (ASTM 1020) casing. While one side of the magnet is in contact with the continuous steel shell, the other side is in contact with a field guide, which directs the majority of the magnetic field in the magnetic circuit out radially through an air gap into the steel casing, where it is directed back to the other side of the magnet. It is in this air gap that the moving coil assembly of the actuator is located. This coil assembly consists of 0.321 mm diameter (28 gauge) magnet wire wound 6 times around a former made of Torlon, a thermally resistant, performance thermoplastic. The length of the coils was such that there would be coil present in the air gap between the field guide and steel shell during the whole desired stroke of the actuator. This resulted in a coil 38 mm long, with a resistance of approximately 11.8 Ω.

The coil is wound in the former to maximize the amount of conductor in the air gap. To maximize this space further, the plastic former serves as the linear bearing for the actuator as well. The former slides on its outer surface, with the inside of the steel shell serving as the guide. The front end of the former has been adapted to attach to the piston of a syringe and piston assembly from a commercially available jet injector (Injex^{TM}, INJEX Pharma Ltd., Miama, FL) [5]. The syringe, or ampoule, is attached to the front plate that is attached to the steel housing. Thus, the relative movement of the coil with respect to the steel shell due to Lorentz forces drives the piston towards the end of the ampoule.

2.3 Modified Benchtop Setup

Construction of a benchtop jet injector device provided an opportunity to add various sensing improvements to the current iteration of the device. The benchtop device to

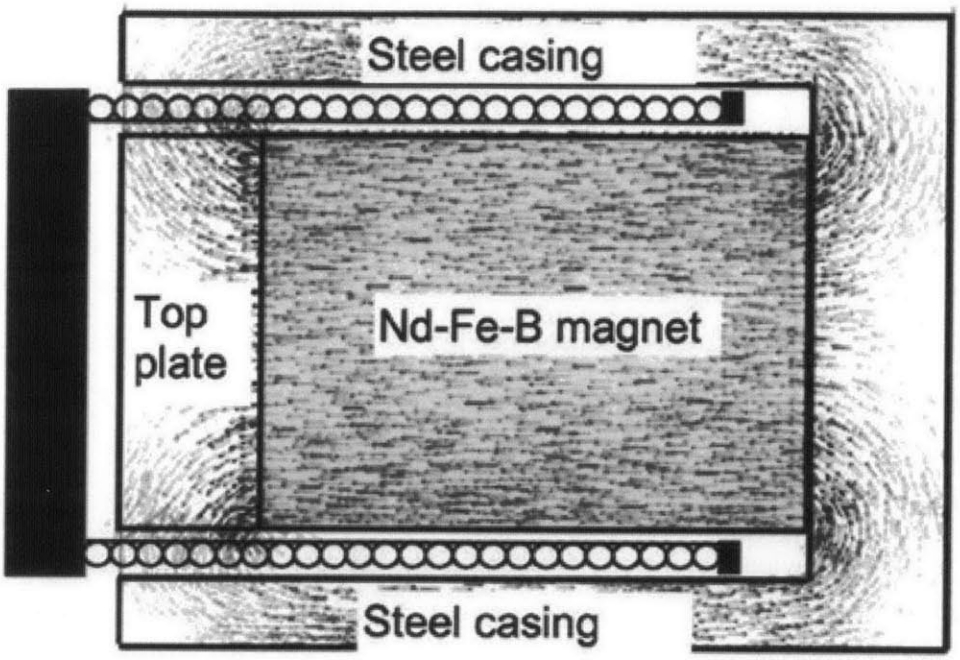

Figure 2-1: A schematic of the magnetic circuit used in the custom Lorentz-force actuator. The black dashes represent the magnetic flux lines travelling through the circuit. Reproduced from [23]

be manufactured was based on the state of the art design presented, but was modified to mount a PCB that would house additional sensors. These sensors were a linear encoder [27] for precise position measurements, a Hall effect sensor [28] to detect the presence of the far-field effects of the magnetic circuit, and a thermopile [29] to measure the coil temperature inside the motor.

2.3.1 Sensor Positioning Considerations

All sensors needed to be placed on a single PCB mounted along the outside shell of the Lorentz-force motor. This meant removing part of the outer steel shell in the existing motor design to allow for a flat mounting surface. As illustrated in Fig. 2-2 each sensor needed to be mounted in a specific position: the linear encoder and the thermopile needed to be placed so that they had a view of the moving coil at all times, meaning that they needed to be as close to the middle of the motor's stroke as possible. The Hall effect sensor needed to be placed far enough away from the magnetic circuit so that its measurements were not saturated, but still close enough that far field effects would still be measurable. Additionally, placing the PCB in the middle of the stroke came at the cost of removing steel material used in the magnetic circuit of the device, potentially weakening the magnetic field. Lastly enough material had to be removed from the shell so that the linear encoder and the thermopile were within their working distances. The linear encoder needed to be within 0.5 to 1 mm of the encoder strip to provide repeatability, while the thermopile had to be placed so that the majority of its field of view was not obstructed by the steel housing.

Placement of the Hall effect sensor was determined during its calibration. The Hall effect sensor was positioned at varying distances from a rare earth neodymium magnet, and the resulting voltage was measured. Additionally, the magnetic flux desnity was measured at each point using a portable Gaussmeter [30]. This allowed for both calibration of the sensor as well as a proper indication of the distance at which the magnetic field saturated the sensor. The results of the test are shown in Fig. 2-3. The sensor saturated at a distance of approximately 20 mm from the magnet. Once the approximate sensor position had been decided, measurements of the

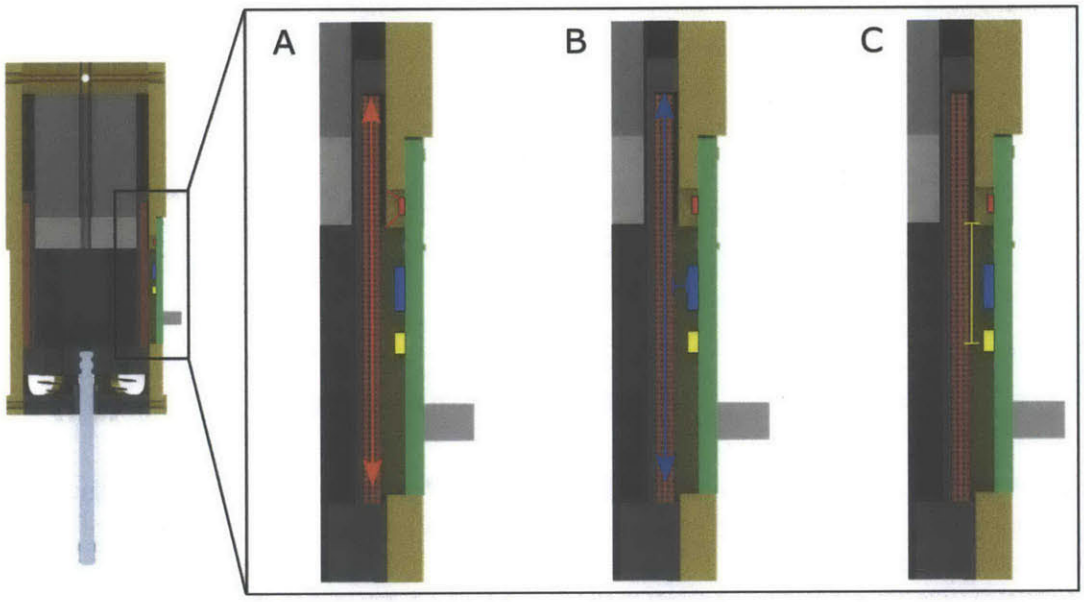

Figure 2-2: Placement considerations for each sensor. (A) The thermopile must be placed so that it is in view of the coil over the full stroke, and its view is not obstructed by the steel shell. (B) The linear encoder must also be placed so that it is in view of the coil over the full stroke of the injector, and it must be within a certain distance from the encoder strip mounted on the coil. (C) Lastly, the hall effect sensor must be far enough from the magnetic circuit so that it does not saturate, but near enough to pick up stray effects of the field.

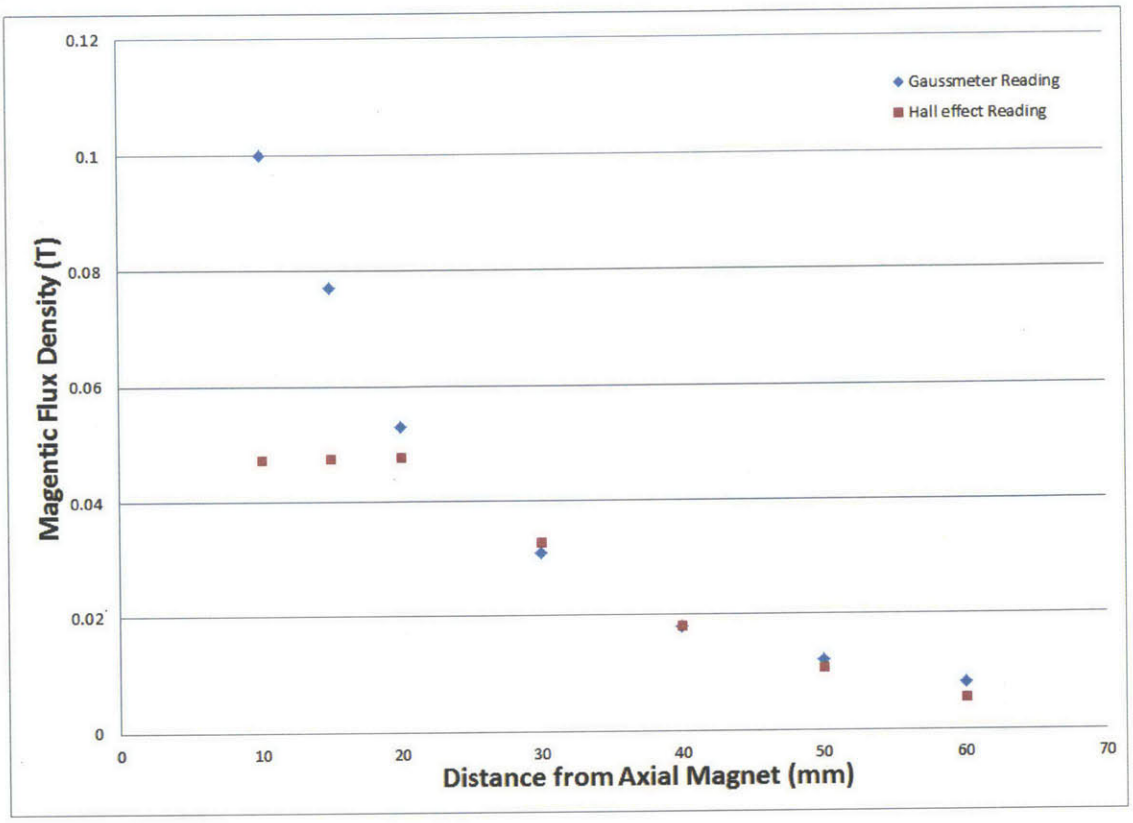

Figure 2-3: Calibration results of the Hall effect sensor. The sensor saturates at approximately 0.05 T at a distance approximately 20 mm from the face of a N50 neodymium magnet.

magnetic flux desnity at that position were performed to ensure that the positioning was appropriate. The resulting magnetic flux density was 0.020 T, approximately half of the full range of the sensor. This magnetic field is lower than those measured in the calibration tests because the magnetic circuit of the actuator directs most of the field away from the sensor.

Creation of the window for the thermopile provided another challenge. Because the thermopile had to be placed in a region that was in view of the coil at all times, material from the part of the shell responsible for the magnetic circuit had to be removed. The window through which the thermopile could view the coil had to be just wide enough so that the shell did not obstruct the field of the view of the thermopile: any wider would result in unnecessary material being removed, potentially weakening the magnetic circuit of the motor. The center-most 126.8° in the field of view of the

sensor accounted for 90% of the thermopile signal [31] (see Fig. 2-4). As a result, a window 4 mm wide was cut into the shell to ensure that the sides of the window did obstruct the relevant field of view of the thermopile. The final PCB design is shown in Fig. 2-5.

2.3.2 Modifications to the Existing Shell

Having made the appropriate calculations, a 16 mm wide face was milled on one side of the shell, with the cut being 1.5 mm deep, and extending 8.25 mm into the portion of the shell used for the magnetic circuit. Additionally, to allow space for the linear encoder strip to slide throughout the travel of the coil, a 9 mm wide cut 0.75 mm deep was made into the shell using a wire EDM [33]. The magnetic circuit was then assembled and the resulting magnetic field in the air gap between the field guide and the outer shell was measured. The resulting magnetic field was approximately 0.6 T, the same value as measured in previous iterations of the device, indicating that the modifications to the shell did not greatly affect the quality of the magnetic circuit in the motor. The final CAD design and the manufactured device are shown in Fig. 2-6.

2.4 Flexible Wire Elements

Besides increased resolution, one of the proposed advantages of using a linear encoder over a potentiometer is that it is a non-contact sensing method. Because there is no connection between the position sensor and the moving coil, friction or damping caused by the fit or sliding of the potentiometer is eliminated. However, if this advantage is to be fully realized, all other unaccounted forms of drag on the coil need to be eliminated as well. Another significant contribution to drag is the tugging force of the wires that provide current to the moving coil. Besides providing drag, the moving cables were prone to mechanical fatigue due to the constant accelerations and decelerations of the coil, and required a set clearance around the motor, making packaging a housing around the motor difficult as well. In summary, a solution

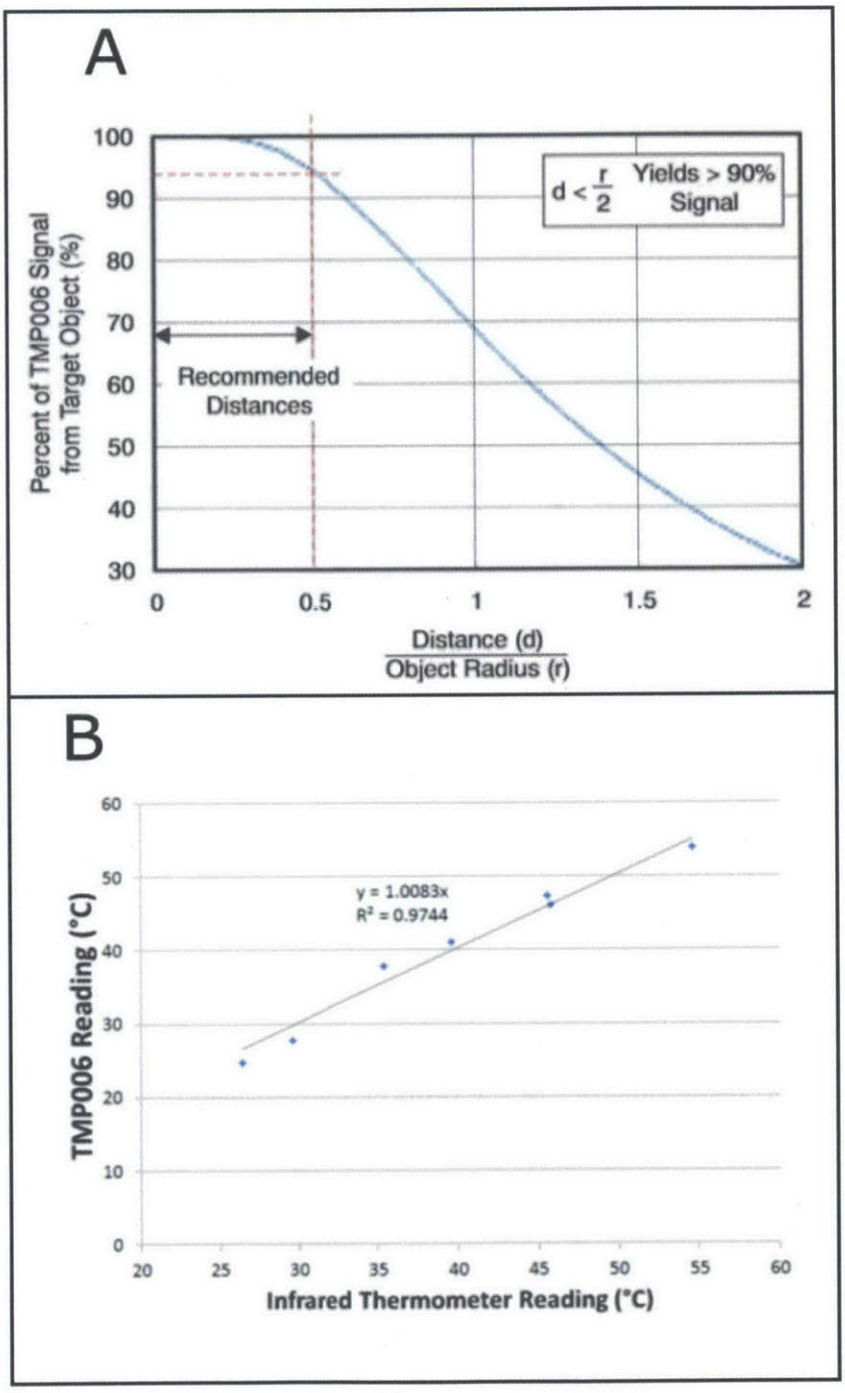

Figure 2-4: Relevant thermopile information. (A) The depth of the window in the housing was less than a quarter of its width to ensure only the coil was in the thermopile's field of view (taken from [31]). (B) The results after calibrating the thermopile when compared to a Fluke IR thermometer [32].

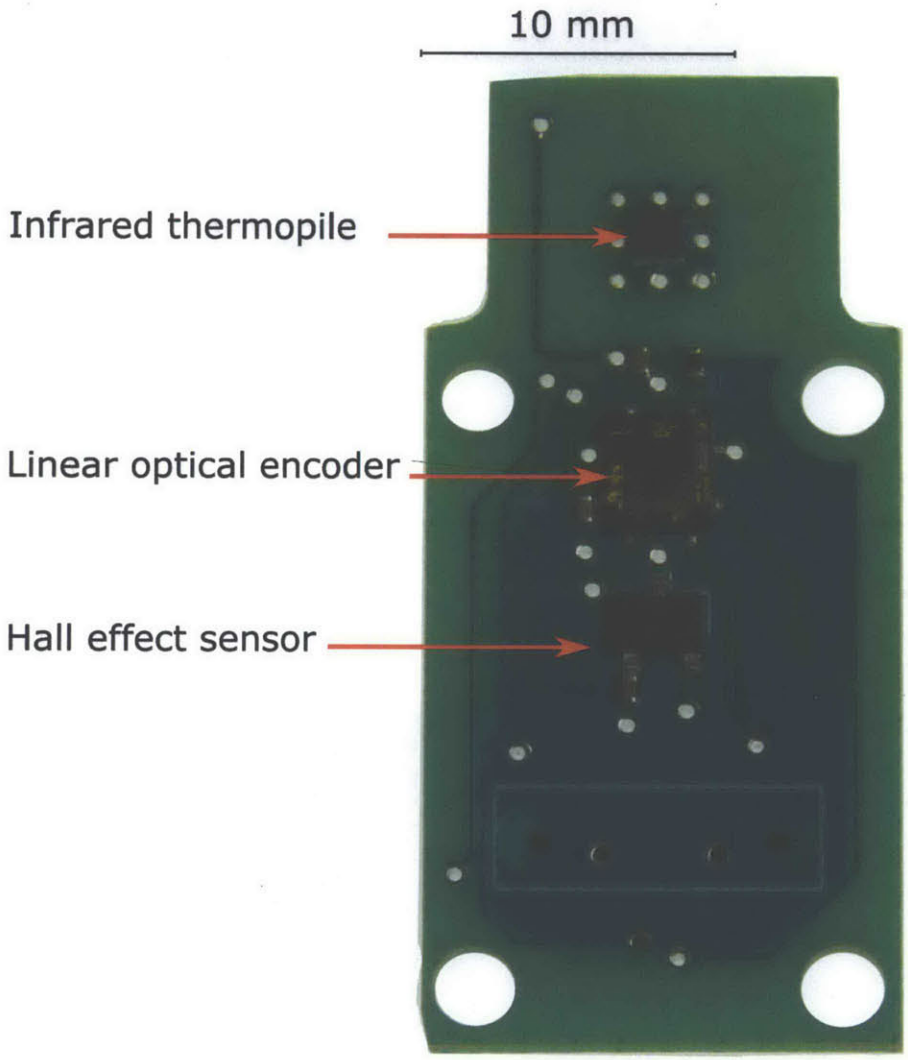

Figure 2-5: Final PCB with Hall effect sensor, linear encoder, and thermopile

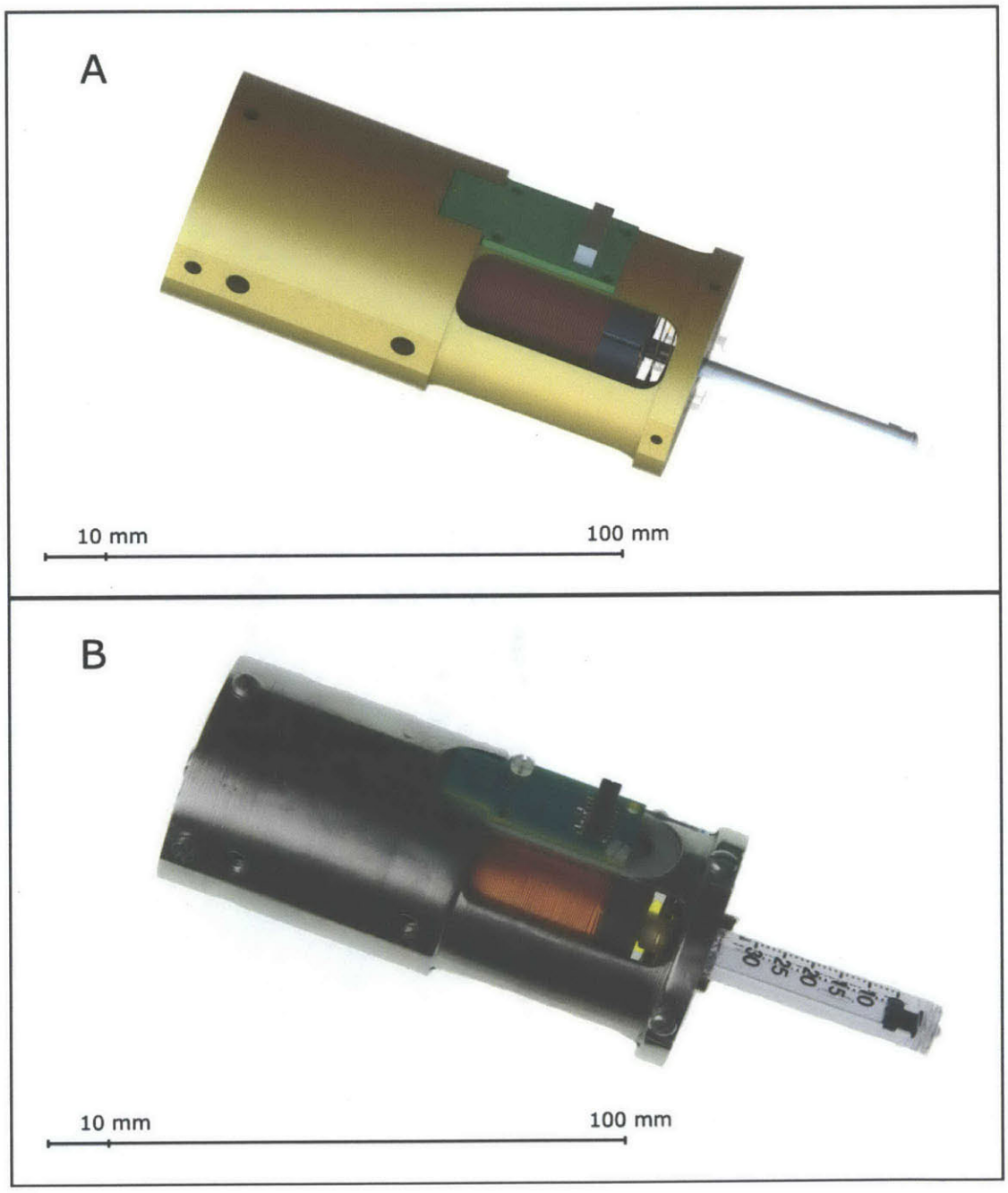

Figure 2-6: Perspective view of the (A) modified jet injector CAD and (B) manufuactured and assembled jet injector. Gold plating was not included

was needed that eliminated the strain of the moving wires while creating a lower profile. The solution was to create a flexible coil element that attached from the front of the moving coil to the fixed front plate as shown in Fig. 2-7. Wires from a power amplifier could then attach to this front plate and remain stationary while the flexible coil elements would fold in and out as the coil moved. While these coils could provide a slight spring-like resistance to the moving coil, their drag and mass would be significantly less than the attached wires from the previous design.

2.4.1 Flexible Element Design

The spatial limitations in the inside of the motor proved to be the biggest design constraints for the flexible wire elements. To ensure no enlargement in the profile of the motor, the flexible elements had to be completely contained inside the motor, between the moving coil and front plate. Additionally, for ease of assembly, it was desired that the coil elements be printed out of 1 planar sheet of flexible PCB material. These constraints led to a helical design intended to maximize the extendable length of the elements.

The width of the wire trace was determined to be 3 mm for a flexible PCB with standard 1 oz copper clad. Using a copper current carrying capacity of 10^8 A/m^2 for short durations, 10.5 A was the most current that could be provided at kilohertz frequencies to ensure that there was no fusing of the copper. However, it is important to note that the general current carrying capacity is assumed for a circular conductor. The current carrying trace is long and flat, and even with once side adhered to a flexible backing, has approximately 250% more surface exposed than a circular wire of equivalent cross sectional area. Because the danger of copper fusing is inversely related to the amount of heat the conductor can dissipate, increasing this surface area increases the current carrying capacity. Additionally, traces were printed on both sides of the flexible PCB material, increasing the current carrying capacity even further. This gave us a factor of safety of at least 2 over the maximum assumed current of 30 A through the coils. These flexible coils have been tested up to 50 A without any fusing occurring.

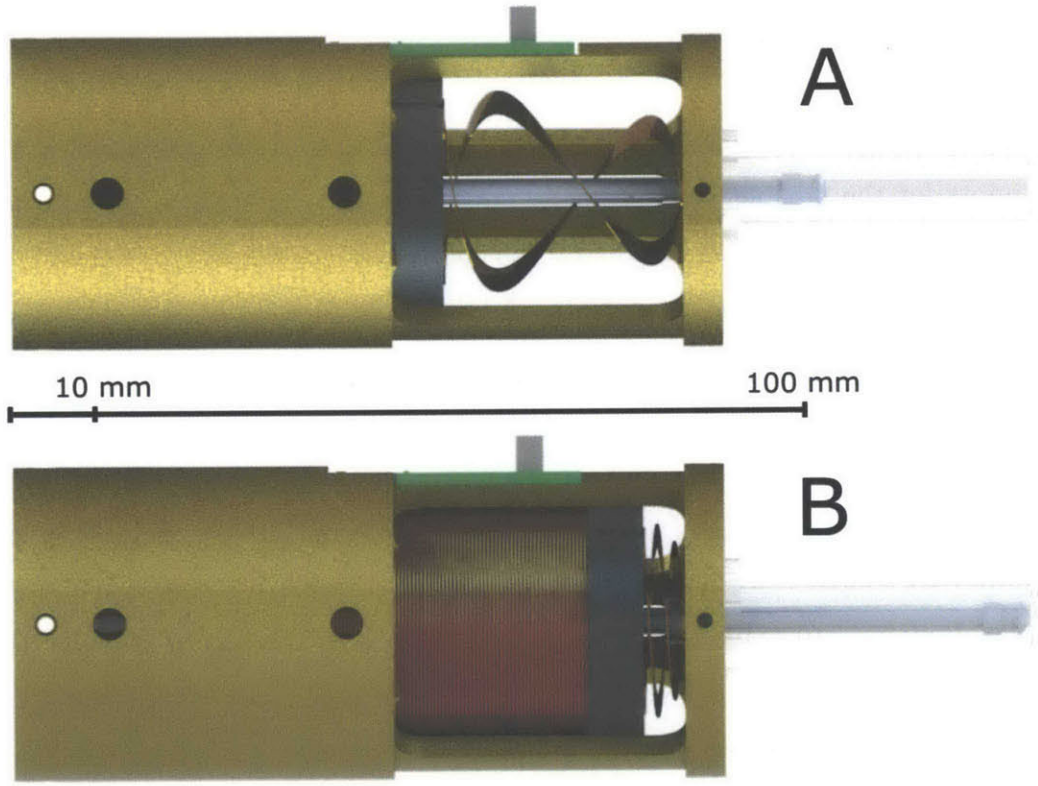

Figure 2-7: Rendering of the flexible PCB elements in the (A) fully extended and (B) folded configurations.

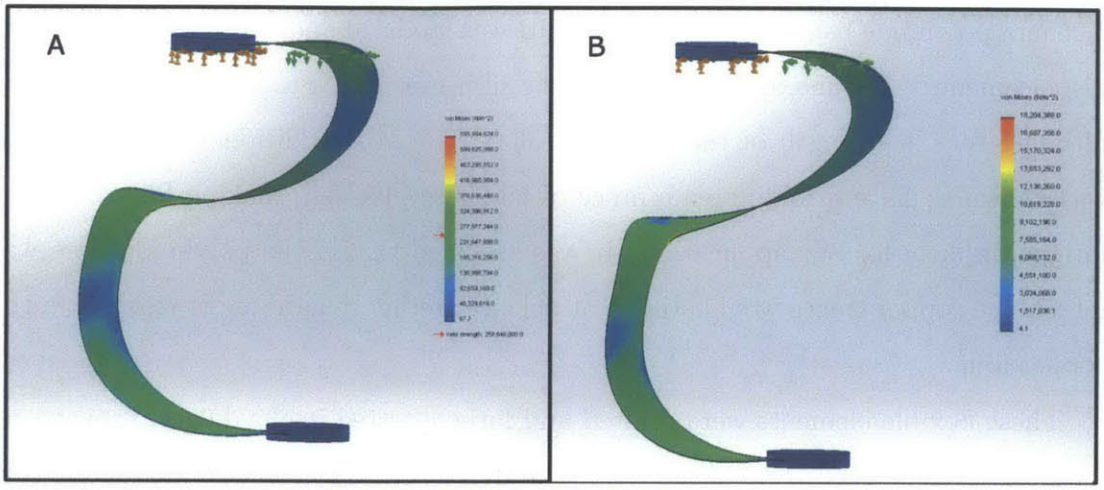

Figure 2-8: FEA analysis of the bending of the flexible PCB elements. (A) A 0.0035 mm copper foil was displaced 30 mm to simulate the stresses on the copper trace. The majority of the stresses were above the general yield stress of copper. (B) A 0.0508 mm polyimide film was displaced 30 mm to simulate the stresses on the Kapton backing of the flexible PCB. The maximum stress on the coil was 18.2 MPa, roughly half of the ultimate tensile strength of Kapton [34]. All tests were done using SolidWorks Simulation Nonlinear Analysis FFE Plus Solver [35]

2.4.2 FEA Analysis

To determine whether the flexible coils would fail mechanicaly during use, the mechanical stresses in the material intit is fully extended position were solved for using FEA modeling in SolidWorks [35] (see Fig. 2-8). A flexible PCB consists of many layers: thin copper film is adhered to a backbone of polyimide film, along with outer coverings. It has been shown that the copper films endurance limit is increased by the presence of this polyimide film and outer coverings, which essentially bridges any cracks in the copper and prevents their propagation [36]. As a result two model simulations were done. First, a 0.35 mm thick copper film was modeled, and the resulting stress when stretched 30 mm was modeled using a nonlinear analysis with the FFEPlus solver with large displacement considerations. The majority of the copper film was subject to stresses around 250 MPa, around the ultimate tensile strength of the material. However, this did not necessarily indicate failure, as the actual flexible PCB is a composite in which the copper film is just one material. Next, the

0.05 mm polyimide backbone of the flex PCB was modeled and subjected to the same displacements. The maximum stress on the film was 18 MPa, a little over half the ultimate tensile strength of the material (36 MPa) [34]. Additionally, the material was known to have a folding endurance of 55,000 cycles [34], making failure due to fatigue unlikely for our application. It was assumed that if the polyimide base was intact, the copper traces would still be attached together, regardless of yielding in the copper film.

These flexible elements were printed and fatigue tested in the device, showing no failure after 2000 cycles. As of the writing of this thesis, the coils have not shown any failure as a result from fatigue or wear.

2.5 Design of a Smaller Lorentz-Force Motor

2.5.1 The effects of scaling a motor geometry

One of the largest obstacles towards the commercialization of a Lorentz-force based needle-free injector is the size and weight of the current motor. While the current motor serves well for bench level tests, it is too large and heavy to be used in a portable device. While previous work has been done at length in creating various optimum geometry Lorentz-force motors for use in jet injection [37] [38], a smaller, simple, low-cost, proof of concept design was desired. One possible solution was a scaled down version of the current device. For any Lorentz-force actuator, the force output of the device could be modeled using the following equation:

$$F = B \times Il = B \times \frac{Vl}{R}, \tag{2.1}$$

where F is the Lorentz force, B is the magnetic flux density. I, V and R are respectively the current going through, voltage across, and resistance of the conductor, and l is the length of the conductor in the magnetic field. By reducing the diameter of the inner magnet by half, the average magnetic flux density in the air gap is reduced by half as well. While the the resistance of the coil is also cut in half, this is offset

Parameter	Effect of scaling motor diameter by half
Resistance	$\frac{1}{2}\times$
Length of conductor in magnetic field	$\frac{1}{2}\times$
Magnetic flux density	$\frac{1}{2}\times$
Force for particular voltage	$\frac{1}{2}\times$
Power consumed at a particular voltage	$2\times$
BL constant	$\frac{1}{4}\times$
Motor constant	$\frac{1}{2\times\sqrt{2)}}\times$

Table 2.1: Effect of relevant parameters by reducing motor diameter by half

by fact that the the length of conductor in the magnetic field also reduces by half, resulting in half the force output for a given voltage. An additional drawback would be that while the force output at a given voltage is halved, the energy dissipated at a that voltage doubles. This means that if the current motor size is reduced by 50%, the motor constant, the force per square root of power consumed, is reduced by 35%, meaning that the smaller motor is less efficient. However, both the energy dissipated (80 J) and peak force modeled (180 N) were deemed acceptable for injection into human skin for the current ampoule design [39]. The resulting motor has a mass of 200 g, 50% of the original motor mass, and was 28.7 mm wide, 70% of the original size.

2.5.2 FEA Modeling and Experimental Results

The force output of both both the smaller and original Lorentz-force motors were modeled using COMSOL Multiphysics [40]. The model was an axisymmetric model in which the shell and field guides were modeled as soft iron. It was assumed 75% of the area attributed to the coil was filled with conductor, a reasonable estimate for a well-wound coil. Both the magnetic field and force output at various voltage inputs were modeled. This modeling also provided a way of determining how much material could be taken off the smaller motor diameter without saturating the steel shell. The FEA model used was a modification of one used by Ashley Brown, a master's student in the BioInstrumentation Lab [38].

A smaller motor was constructed based on this model and the relevant parame-

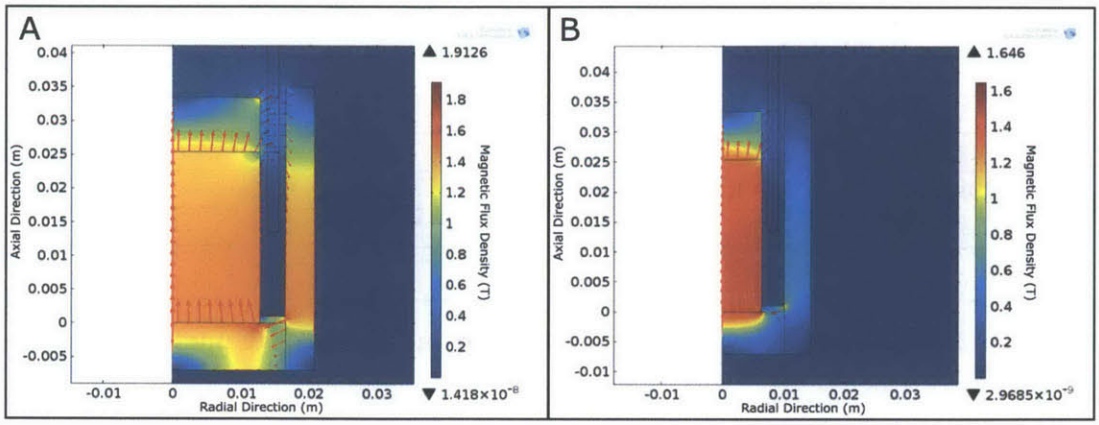

Figure 2-9: Comsol modeling of the magnetic circuit both in the (A) current and (B) smaller Lorentz-force Motor. The current motor had an average magnetic flux density of 0.53 T in the air gap, while the smaller motor had an average flux density of 0.26 T.

ters were measured. The magnetic flux density in the air gap was measured to be approximately 0.28 T compared to a modeled value of 0.26 T. Force outputs for the larger motor had been performed using a 20 ms step input on a standard push button load cell [41]. However, because of the higher currents running through the smaller motor, a much smaller 6 ms step input was used, and a dynamic load cell [42] was used to capture the force output. The test setup is shown in Fig 2-10.

In both cases, the resulting force outputs of the constructed motors were approximately 80% lower than the modeled results. This could be partially due to the manner in which the coil was wound, as the resistance of the coil was lower than expected for a perfectly wound coil. However, these lowered resistances should only account for a 5% decrease in expected force output. The rest of the discrepancy could be due to misalignment of the motor or an overestimate of the magnetic flux density. While initial measurements indicated that the measured magnetic flux density was slightly higher than the expected flux density, this measurement is extremely sensitive to precise positioning of the Gaussmeter. The actual flux density could be lower because the shell was actually made out of a low carbon steel, rather than a soft iron.

As shown in in Fig 2-11, the maximum recorded force output of the smaller motor was 130 N. While this force ouput (given the use of the Injex^{TM} [5] ampoule), is large

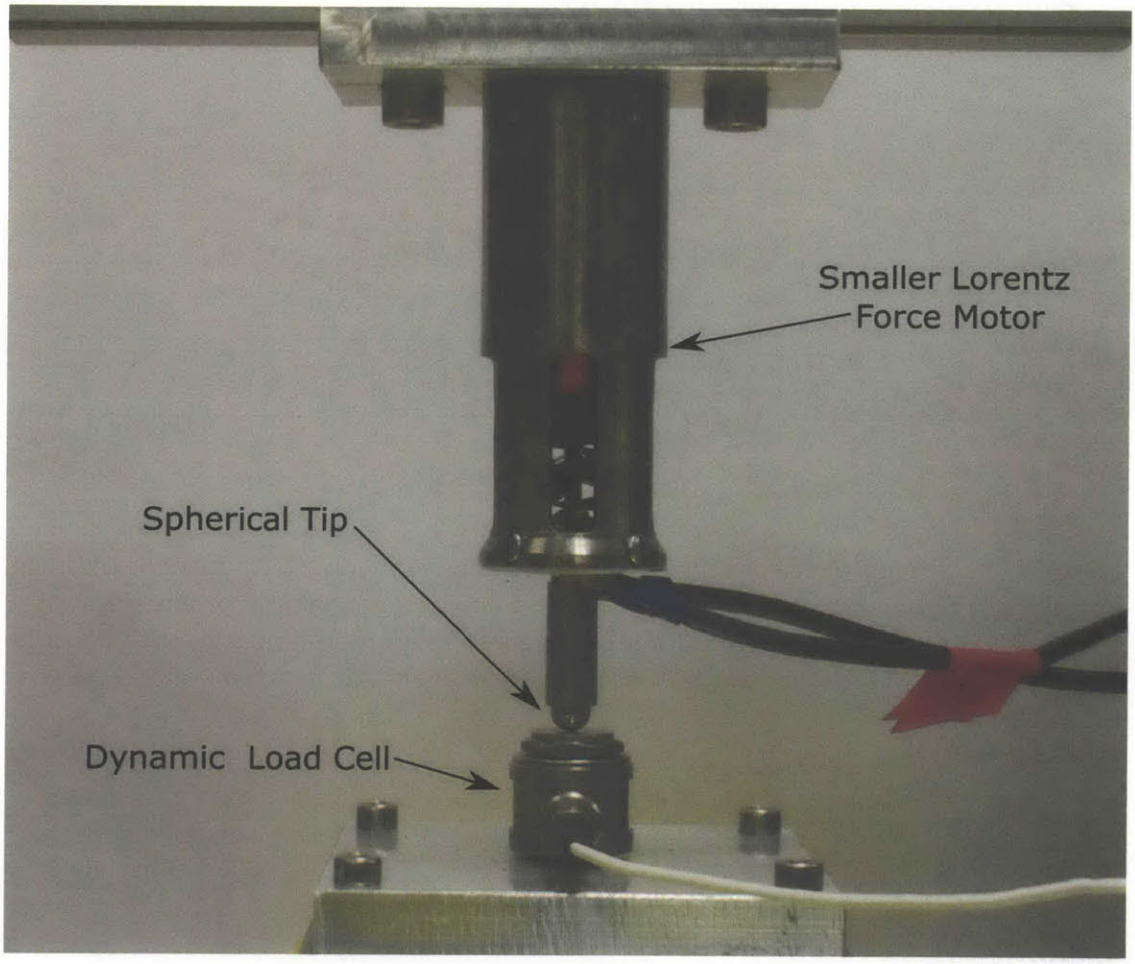

Figure 2-10: Testing setup for measuring the static force output of the smaller Lorentz-force motor.

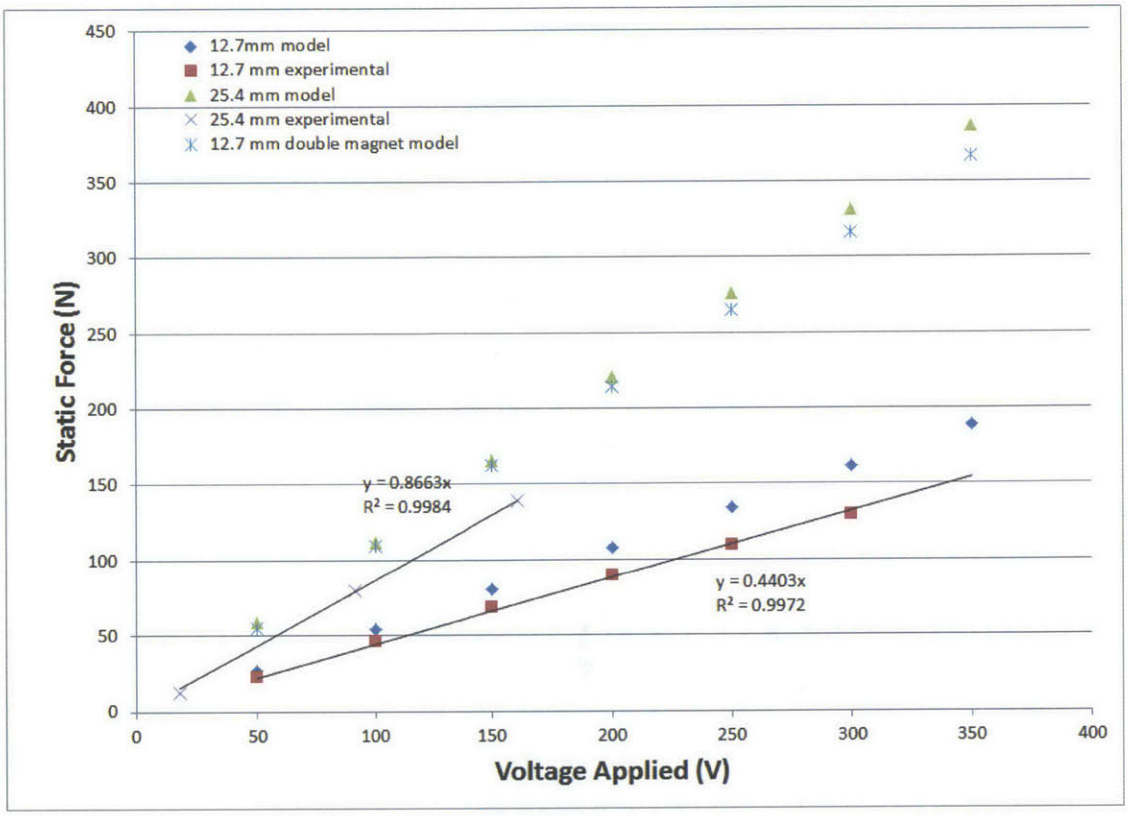

Figure 2-11: Summary of both modeled and experimental force outputs. For both the larger and the smaller motor, the measured force outputs were approximately 80% of the expected force outputs. A double magnet design motor would have the same diameter as the smaller motor, but would provide a similar force to voltage ratio as the larger motor.

enough for some human applications, it is not large enough to consistently pierce human skin [39]. However, a simple solution is present in a double magnet design (Fig. 2-12), which would approximately double the magnetic flux density doubled to force output of the motor at the cost of length. Such a design was modeled to be able to provide up to 275 N of force at 300 V, the maximum rated output of the linear amplifiers being used. Additionally, this would improve the motor constant to 71% of the original design.

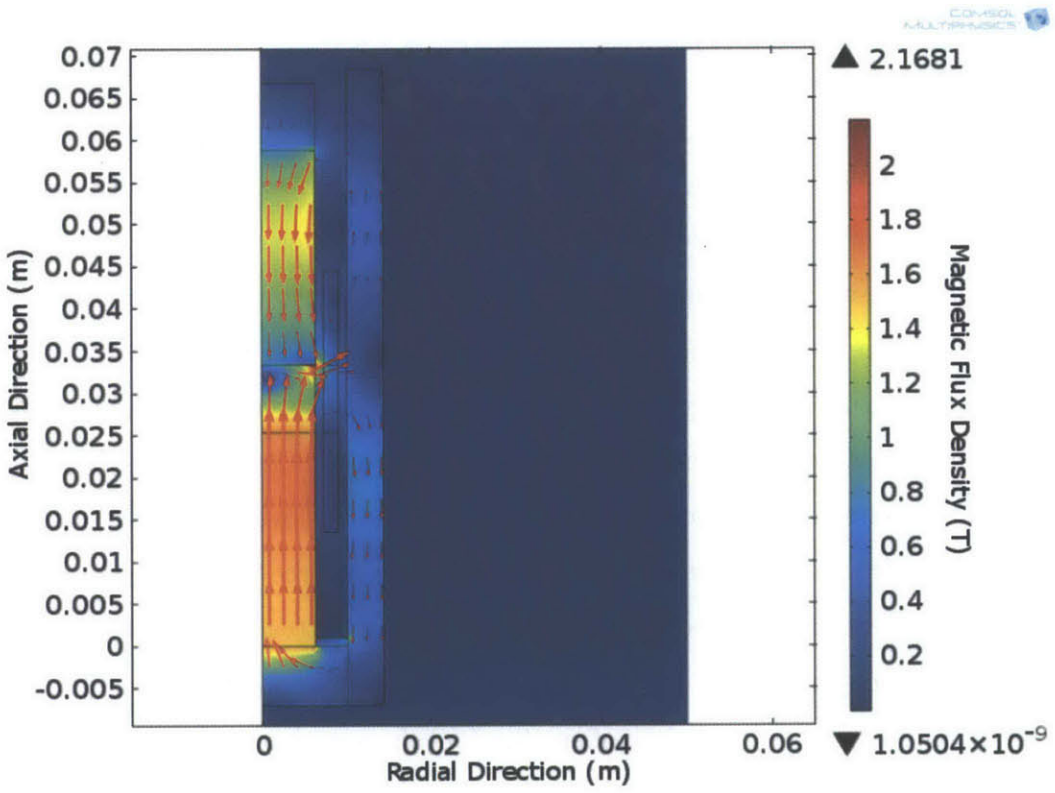

Figure 2-12: Comsol modeling of the magnetic circuit for a double magnet design for the Lorentz-force Motor. The motor has an average magnetic flux density of 0.50 T in its air gap.

2.5.3 Scaling Considerations of the Design

All of the sensing and cabling improvements made on the earlier benchtop device were replicated on the smaller motor. Certain design improvements were made as well. For example, to reduce cost and time of manufacturing, instead of requiring an EDM cut on the inside of the shell to allow space for the linear encoder, a recess was created in the bobbin so that the encoder could fit on the bobbin without affecting the cross sectional profile (see Fig. 2-13).

Scaling issues led to design changes as well. Because of the smaller diameter, the flexible elements inside had a much lower radius of curvature, greatly hindering their compliance. As a countermeasure, the flexible elements were designed so that they were modular and could be attached via solder to another identical coil element, allowing for the use of two flexible coil elements to span the travel of the moving coil instead of just one. Additionally, instead of allowing for a center hole through the magnet and field guide assembly, the magnetic circuit was created with solid magnets, with a recess machined into the endplate to hold the assembly in place along with Loctite 382 [43] thread locker to prevent drift of the magnets over time. These design modifications were able to prove that the original Lorentz-force motor design, as well as the improvements introduced in this thesis, are scalable to a smaller motor.

Work by others has been done to package this smaller motor along with the necessary components into a variety of smaller form factors that are more acceptable for consumer use.

2.6 Conclusion

Various improvements have been made to the current design of the needle-free injector to make it a more viable product. A Hall effect sensor and a thermopile were added to provide critical safety and quality checks on the actual motor, and a linear encoder provided increased position resolution. Additionally, flexible PCB elements reduced drag on the coil while eliminating a former failure mode due to the moving cables. Lastly, it has been shown that all these improvements could be successfully scaled

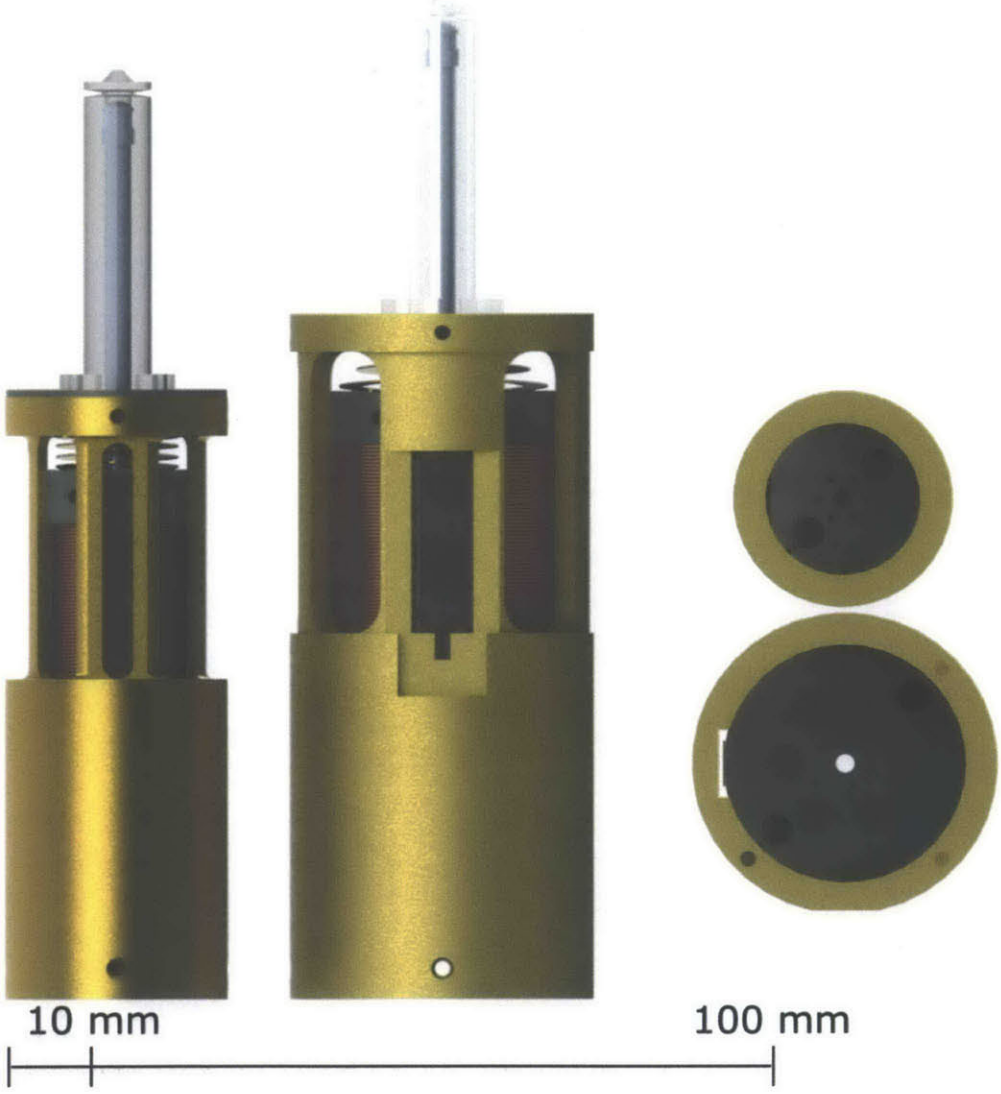

Figure 2-13: Longitudinal (left) and axial views (right) of the larger and smaller motors.

down to an actuator half the size of the current actuator, and that this actuator would provide sufficient force for use in needle-free injection.

Chapter 3

Precision Volume control

The current needle-free injection system has been used to deliver up to 50 µL of fluid with a precision of 0.5 µL [15]. While this is acceptable for injections of insulin or lidocaine, where injections are typically over 100 µL, [10] [11] [12], this error is noticeable when smaller deliveries on the scale of 10 µL are desired. One such application would be injection of drug at multiple sites, theoretically increasing the rate of absorption and efficacy of the drug. An increase in the precision of the volume delivered will make the Lorentz-force based needle-free injection device more versatile.

3.1 Possible Sources of Volume Error

One possible reason for loss in precision of drug delivered could be the compression and expansion of the polycarbonate ampoule. Because this effect causes an increase or decrease in the cross-sectional area of the fluid channel, the magnitude of this error is not constant, but proportional to distance traveled by the piston and thus volume delivered.

From *Roark's Formulas for Stress and Strain* (Fig. 3-1) [44], the estimated loss of volume delivered due to this effect is only 5.262 $\times 10^{-5}$µL per µL delivered, and is not dependent on the starting position of the ampoule. For the time being, effects due to an elastic ampoule were ignored as they should theoretically not affect the steady-state values for the amount of volume delivered.

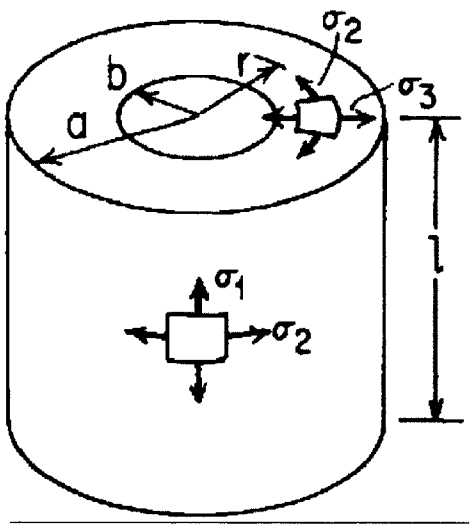

Figure 3-1: Diagram from *Roark's Formulas for Stress and Strain* [44] for a thick walled cylinder.

Another possible source of error could be compression of the rubber tip on the piston. At atmospheric pressure, the fluid inside the ampoule would be able to compress the piston tip. This tip has been experimentally determined to have as stiffness of 200 kN/m [45], resulting in a compression corresponding to a loss of 0.05 µL fluid delivered. However, once again this is a steady-state offset which should theoretically not affect the precision of volume delivered.

One more source of error would be in the current position sensing of the coil, which is assumed to have a direct relationship to the amount of fluid in the ampoule. Currently, a linear potentiometer is being used to sense position. When given a 10 V reference signal, the slope of the signal was approximately 3.3365 mm/V. However the steady-state error had a noise of 0.025 mm. The linear error of the potentiometer was 0.5% [25], which for the 30 mm potentiometer corresponded to 0.15 mm. With just these two sources of error, the error of the potentiometer was at least 152 µm. This corresponded to a maximum error in volume delivered of up to 1.52 µL during drug delivery. Once again, while this may be an acceptable amount of error for 100 µL

injections, it could be potentially problematic when 10 or 20 µL injections are desired.

3.2 Finer Position Sensing

3.2.1 Possible Sensing Options

Many different sensing options could provide an increase in precision in measuring coil position. Both laser interferometers and position sensitive diodes were too costly and unrealistic to package and keep aligned in a portable device. Linear variable differential transformers (LVDTs) could provide both the resolution and range desired, but the presence of the actuator's magnetic field could cause position drift. Capacitive sensors could also be a viable option, but they provide significant tradeoffs between range and precision due to the inverse relationship between capacitance and distance. Optical encoders are a possible solution: they are potentially very low profile, have little to no tradeoff between range and precision, and would not be as affected by the high currents and changing magnetic fields generated during an injection.

3.2.2 Optical Encoder Fundamentals

At its crux, an optical encoder is a photodiode measuring the intensity of a light passing through an evenly spaced grating of known scale (see Fig. 3-2). As the scale is moved, the light the photodiode receives is either blocked or allowed to pass through. By counting the number of times the intensity of light cyclically increases and decreases, it can be inferred how much the grating and sensor have moved relative to each other. To determine the direction of the relative movement, a second photodiode is placed 90° out of phase from the first photodiode. Depending on which photodiode's waveform is following which, the direction of relative motion can be inferred as well.

As shown in Fig. 3-2 there are 4 different permutations for the high or low intensity of light on each photodiode, corresponding to a movement equivalent to a quarter of the grating spacing, commonly referred to as a "tick" of an encoder. The output of an

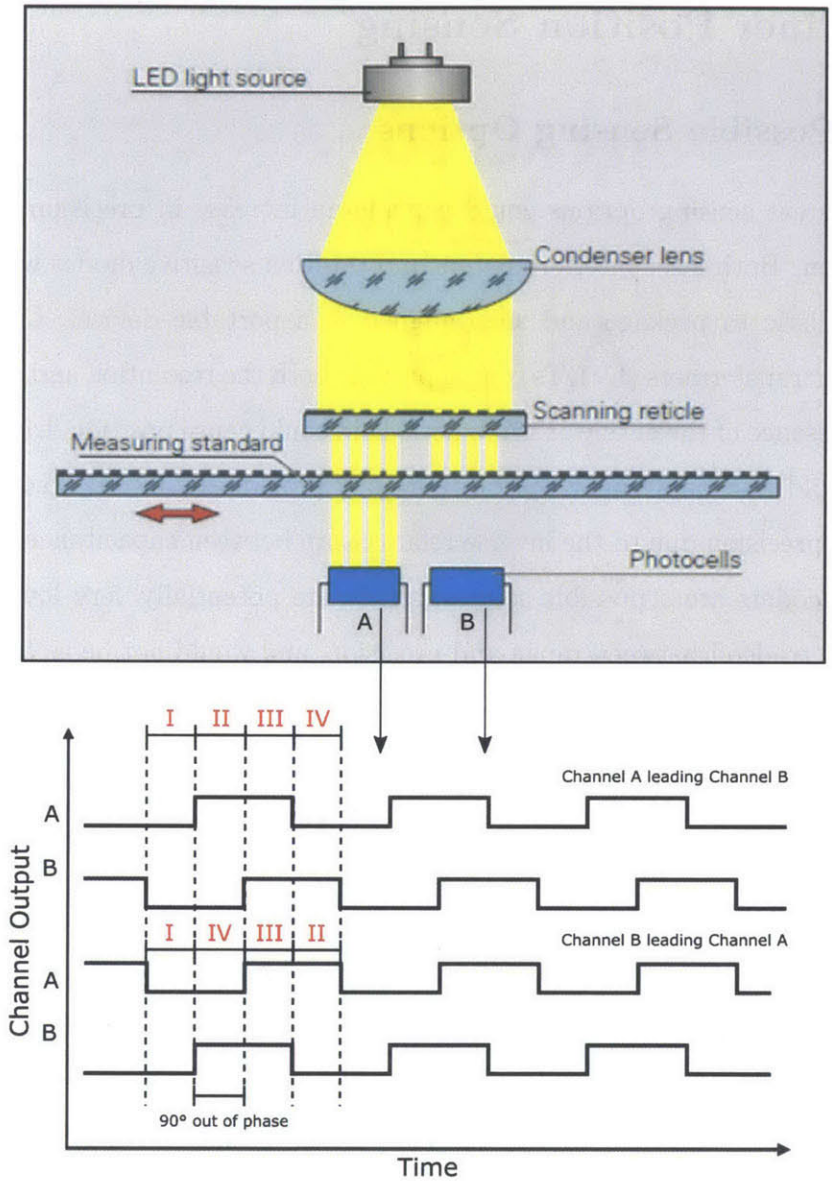

Figure 3-2: Diagram of an optical encoder. (Top) A light source passes through a grating of a standard spacing to a photodiode on the other side (Adapted from [46]). (Bottom) Having two photodiodes 90° out of phase from each other allows for the direction of the relative displacement to be known (Ada[ted from [27]).

encoder is generally two digital signals, each corresponding to one of the photodiodes. As these signals change, the position is incremented or decremented a "tick."

Many encoders now keep the two powered components in the system, the light source (usually a LED) and the photodiodes, on the same surface, and place the grating over a reflective material. Instead of light passing through the grating to the photodiodes on the other side, light is selectively reflected through the grating back to the encoders. This configuration is known as a reflective encoder.

Such a setup is limited in resolution by the spacing of the gratings. Because the two sensors are 90° out of phase, the resolution of the sensor is effectively a quarter of the grating spacing. If greater resolution is desired, interpolation must be used. If the light passing through the gratings is parallelized and the same size as the gap between the gratings, the intensity of light measured by the photodiode is nearly sinusoidal as the light shifts from being fully blocked to fully allowed to pass. Because the two photodiodes being used are 90° out of phase, a plot of the corresponding intensities of light ideally results in a circle (see Fig. 3-3). The ratio of intensities between the two photodiodes can be used to interpolate the relative position in between distinct high and low points of the signal. The plot on which this is graphed is typically known as a Lissajous curve, and is used in calibrating the encoder output. A typical formula to determine the distance travelled between each "tick" is given below:

$$x = d\frac{\arctan\left(\frac{I_B}{I_A}\right)}{2\pi}, \tag{3.1}$$

where x is the position, d is the spacing of the grating, and I_A and I_B are the respective intensities of channel A and B.

3.2.3 Implementing a Low-Cost Reflective Encoder System

A stand-alone high end encoder system ([46] [47] [48]) was not preferable for two reasons. First, the dedicated encoder head is quite bulky, around 15 mm × 40 mm, taking up valuable space. Secondly, the price of these devices and their accompanying grating strips made them prohibitively expensive for use in a mass production,

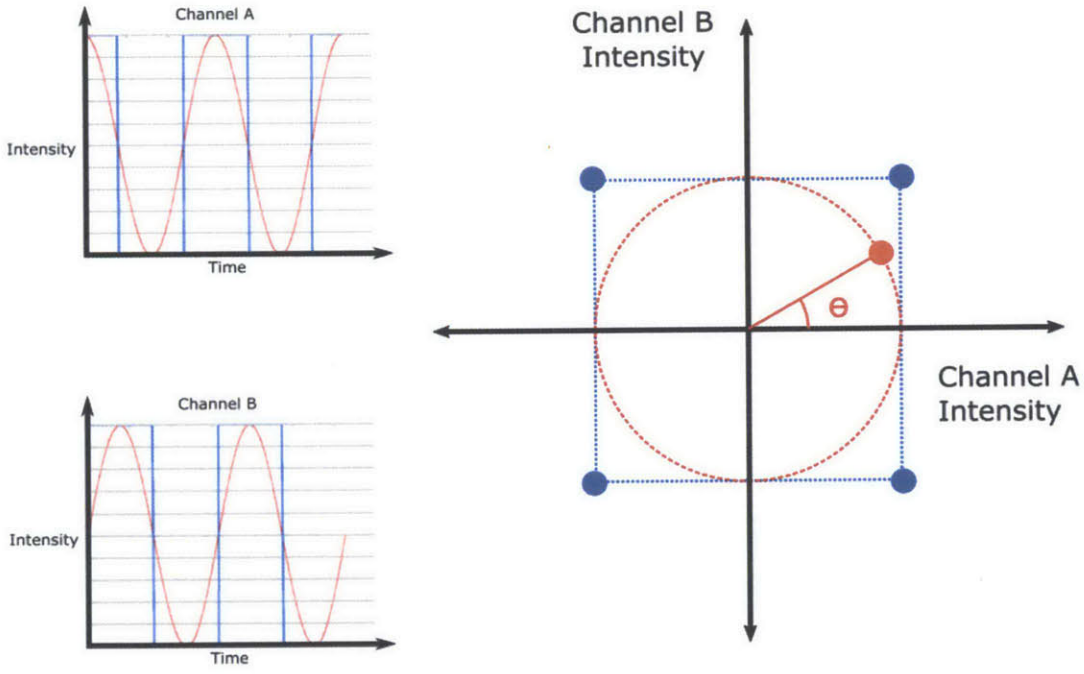

Figure 3-3: A comparison of the digital and analog outputs of an optical encoder. The relative intensities of the two channels can be used to interpolate the encoder position between each digital "tick."

commercial device. A solution based on the Avago AEDR 8500 linear encoders [27] was designed by Adam Wahab, a PhD candidate in the BioInstrumentation Lab. These encoders have a surface mount package size of 3.95 mm × 3.40 mm × 0.96 mm, allowing for the inclusion of other sensors on the same board. Additionally, these chips have up to a 4× interpolation done on the chip itself, allowing for 5 µm position resolution, while still outputting two TTL digital signals. This meant that position could be calculated using standard quadrature encoder hardware or logic.

Because the necessary grating spacing for the AEDR 8500 was only 12 lines/mm, the reflective gratings could be manufactured cost effectively in-house rather than requiring expensive gratings. In additon to being less expensive, in-house manufacturing allowed the production of much thinner gratings. In the current design, the linear encoder grating is fit on the surface of the coil in the clearance between the coil and the shell. A thicker encoder strip would require more clearance between the steel shell and the coil, reducing the strength of the magnetic field that the coil is exposed to.

The encoder strip was manufactured in two parts: a grating pattern and a reflecting backing. The grating pattern was emulsion printed onto a 0.18 mm thick Mylar sheet by a local photo mask company [49]. The pattern consisted of 41.7 µm wide opaque lines spaced 41.7 µm apart, resulting in the required resolution of 12 lines/mm for the encoder. The precise spacing and widths of these lines were a key factor in ensuring proper encoder functionality at higher interpolations. In fact, manufacturing errors that resulted in lines even 2-3 µm thicker than the desired thickness resulted in considerable sensor drift at 4× resolution. To check against any defects in manufacturing, special markings were made every 10 and 100 lines to allow easy measurement of the line spacing (Fig. 3-4). Images of the grating were also taken under 6.6× magnification to determine that the width of each line did not deviate too greatly. The final gratings used in the design had a line width of 42.0 µm ± 1.2 µm with a spacing of 11.9 lines/mm.

These transparent gratings were then attached to a reflective material. Initially, reflective paper and aluminum shim were used, but the combination of striations,

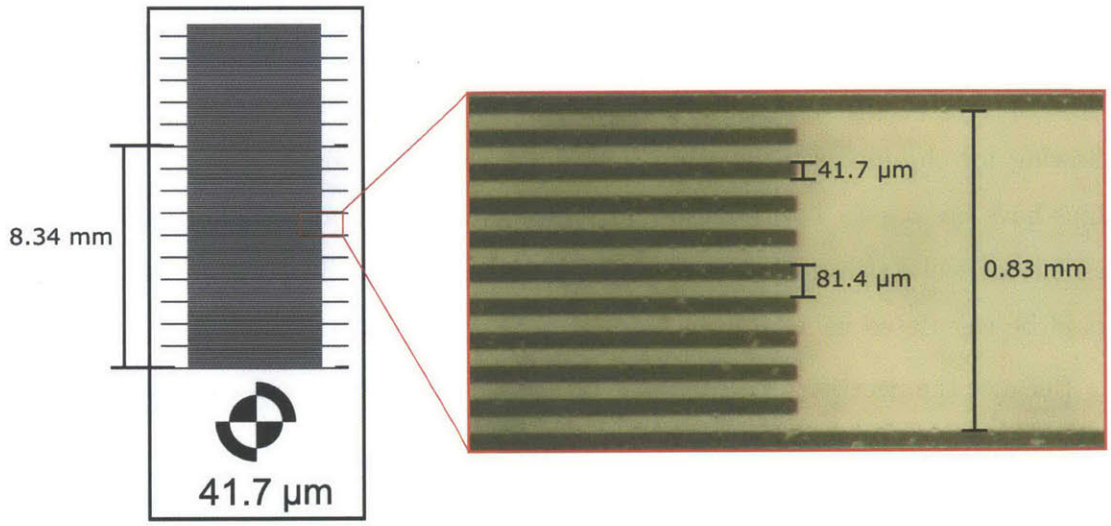

Figure 3-4: The encoder strip was printed on a mylar emulsion. both large scale (left) and smaller scale measurements (right) were performed to ensure the strip was manufactured to tolerance.

crinkles of the material, and stray marks caused during the adhesion process made it difficult to ensure repeatability over a long range of travel. The solution was to sputter coat [50] the backside of each transparency with silver, resulting in a relatively thin and homogenous reflective backing. Each strip was coated for two 10 minute cycles with an ionizing current of 100 mA. The sputter coating process added approximately 2 µm to the thickness of the strip. This strip was then attached onto the coil using Loctite 382 adhesive [43].

Position was calculated from the encoder using basic encoder logic. Depending on the current and previous "states" of the two photodiode signals (see Fig. 3-2), it could be determined whether the coil had moved forward or backward an encoder "tick." Sample encoder logic is shown in Fig. 3-5.

Item	Cost
AEDR 8500	$13.65
Photomask Printing	$1.25
Sputter Coating	$2.08
PCB Manufacturing	$37.00
Total cost	$53.98

Table 3.1: Total cost of implemeting the linear optical encoder system

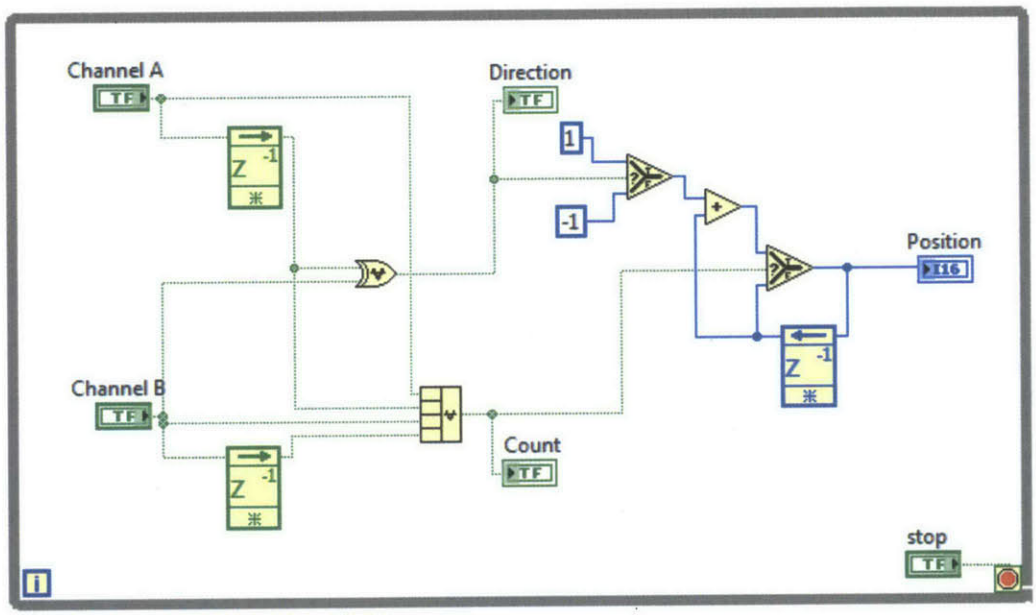

Figure 3-5: Basic logic used in interpreting a quadrature signal from an encoder as it would appear in a LabVIEW block diagram [51]. The current and previous values of the Boolean signals A and B are used to determine whether the encoder strip has moved and which direction it has travelled. This information is used to update a position variable.

3.2.4 Sensor Characterization

Before use in injections, the resolution, linearity, and drift of the optical linear encoder system was characterized. The results are shown in Table 3.2.

Resolution

The resolution of the custom built encoder system was verified using a high resolution (0.25 µm) optical encoder from MircoE systems [48]. The outer shell of the motor was mounted on a micrometer stage, while the usually moving coil on the inside was held fixed. Fine increments on the micrometer stage would move the motor housing relative to the coil inside, allowing for the measurement of very small displacements. The linear scale for the MicroE encoder was fixed on the outside of the shell, with the read head fixed similarly to the inner coil. This allowed measurement from both encoders to occur in parallel, while also allowing the custom encoder system to be characterized as it was intended to be used inside the motor assembly. To determine the resolution of the encoder, the micrometer stage was slowly moved and the distance between each "tick" of the custom encoder system was measured using the higher resolution MicroE encoder. The resulting resolution per "tick" was 21.25 µm $\pm$ 0.44 µm for 1$\times$ interpolation, 9.56 µm $\pm$ 0.54 µm for 2$\times$ interpolation, 4.87 µm $\pm$ 0.44 µm for 4$\times$ interpolation.

Linearity

To test the linearity of the system, the outer housing was once again attached to a micrometer stage, with the inner coil being fixed to allow minute movements of the shell relative to the coil. The micrometer was advanced 20 mm in half millimeter increments, and the number of "ticks" the encoder counted was recorded. The optical encoder system was found to be quite linear, with a slope of 47.9, 95.9, 191.8 "ticks"/mm for 1$\times$, 2$\times$, and 4$\times$ interpolation respectively, and a linearity error of 0.35% over the 20 mm stroke. It is important to note that the measured linearity of the sensor was limited by the precision of the user turning the micrometer stage.

Slight unintended motions by the user could easily cause the readings to be off by a "tick."

Drift

To measure drift of the sensor, the entire jet injector was assembled and the motor was fed a 6 V, 1 Hz square wave for 200 cycles. This signal ensured that the injector would travel its whole stroke in one cycle, lightly hitting an easy-to-measure mechanical stop at the top of its stroke. The position reading (in "ticks") for the metallic stop was compared over the course of the 200 cycle test, which was repeated 3 times. Any drift in the position reading of this metallic stop was indicative of drift of the sensor, meaning that it did not count the same number of "ticks" in the down stroke as it did in the up stroke. The tests revealed little to no drift of the sensor over the 200 cycle test: the drift at each resolution was 0.30 µm/cycle, 0.00 µm/cycle, 0.05 µm/cycle, respectively.

	1× interpolation	2× interpolation	4× interpolation
Resolution (µm)	21.25	9.56	4.87
Linearity (%)	0.35	0.35	0.25
Drift (µm/cycle)	0.30	0.00	0.05

Table 3.2: Sensor characterization of the custom optical linear encoder system

3.3 Use of a Linear Encoder for Precision Volume Control

3.3.1 System Model

Before evaluating the precision of the modified jet injector for actual volume delivery, it was necessary to determine a model to describe the system. The jet injector can be described as a mechatronic system combining the electrical and physical characteristics of the Lorentz-force motor. The two separate models are commonly described as follows:

$$V_s = iR + L\dot{i} + K_e\dot{x}, \tag{3.2}$$

$$K_e i = m\ddot{x} + b\dot{x} + kx, \tag{3.3}$$

where V_s is the supply voltage, R is the coil resistance, L is the coil inductance, i is the current passing through the coil, x is the position of the coil, m is the moving mass of the coil, b is any damping coefficient in the system, and k is any spring-like element in the system.

This leads to an overall transfer function of:

$$\frac{X(s)}{V_s(s)} = \frac{K_e}{mLs^3 + (mR + bL)s^2 + (bR + kL + K_e^2)s + kR}. \tag{3.4}$$

However, since there is little to no springiness in the flexible PCB elements, it is assumed that k is approximately zero, leading to the following equation:

$$\frac{X(s)}{V_s(s)} = \frac{K_e}{s[mLs^2 + (mR + bL)s + (bR + K_e^2)]}. \tag{3.5}$$

All in all, the model to fit our system to is a third order system in which one of the poles is an integrator.

There are two major problems with the use of this model. First, while it is important to note that many of these constants have been experimentally determined, the damping coefficient of the system has not. Moreover, the majority of the damping of the system is due to the friction of the piston in the ampoule, which is not the most repeatable quantity between tests due to deterioration of the piston tip, or between ampoules due to manufacturing changes. As a result, it had to be realized that any control scheme could not be overly sensitive to this parameter. Second, it is important to recognize that the dynamics of the piston tip and ampoule, and their compression and expansion in response to the high pressures during the injections, result in coil position not being necessarily the most accurate estimate of volume delivered or jet velocity in real time. However, because the pressure inside the ampoule returns

to atmospheric pressure when the final volume has been delivered, these effects are assumed to be negligible. While the compression of the piston tip at atmospheric pressure would result in a slight, constant, undershoot, this is not accounted for because it could not be guaranteed that the springiness was a repeatable quantity over the number of injections. This is an unaccounted for disturbance for our system.

3.3.2 System Identification

A sine sweep from 5 to 600 Hz was performed on the jet injector when in 5 µm resolution mode. A 2 pole and integrator model was then fit using MATLAB (Fig. 3-6). The resulting model had an equation as follow, with a percent fit of 85%. At higher frequencies, the piston did not move enough to cause a noticeable change in displacement, and the data for that part of the test was not expected to follow the model, resulting in a low calculation of the model fit.

$$\frac{X(s)}{V_s(s)} = \frac{2.25 \times 10^5}{s(1 + (1.86 \times 10^{-3})s)(1 + (1.71 \times 10^{-4})s)}. \tag{3.6}$$

3.3.3 Control Scheme

When designing a control system for the injector, it was very important that the system tracks desired velocities well, as the velocities at which the fluid is delivered at are critical for injection success [14] [16] [18]. However, due to nonlinearities in the system caused when ejecting a fluid, a simple open-loop or feedback system based on this model does not provide an adequate controller. For example, if the model above is used to predict steady-state velocities, the expected relationship would be a linear relationship between the voltage applied and steady-state velocity. However, open loop tests have found that there actually is a quadratic relationship between the voltage applied and steady-state velocity (see Fig. 3-7) . These nonlinearities are to be expected due to ejection of fluid out of the ampoule.

This relationship was used to create a feed-forward controller for the system based on those designed previously in the lab [15] and further developed by Jean Chang, a

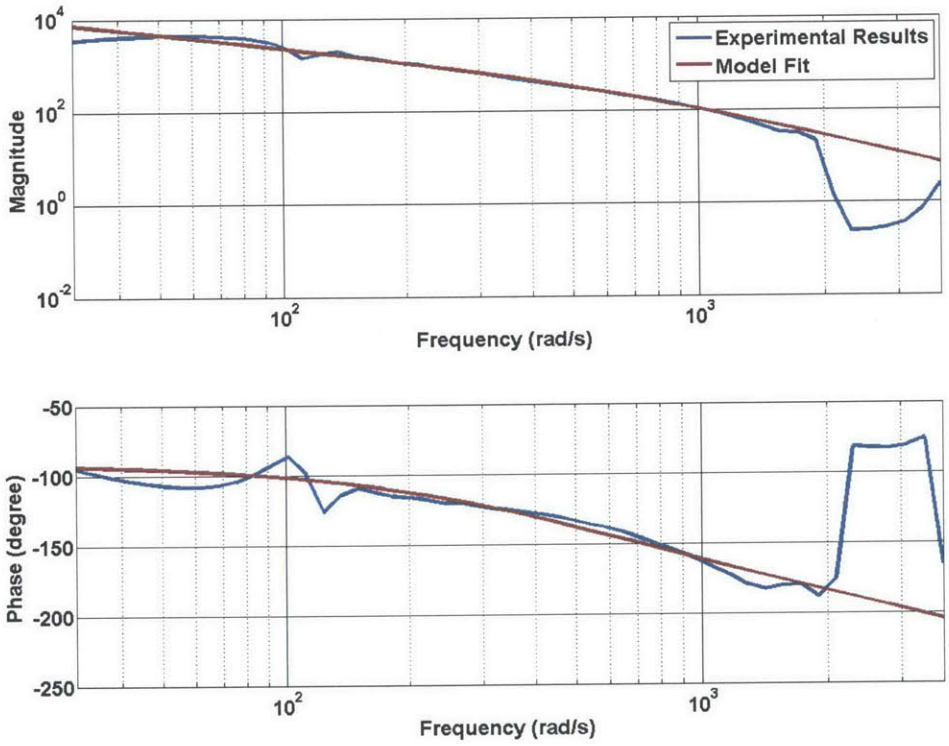

Figure 3-6: System identification of the jet-injector system when no fluid is in the ampoule. The system was modeled as a third order system with no zeros and one of the poles at the origin.

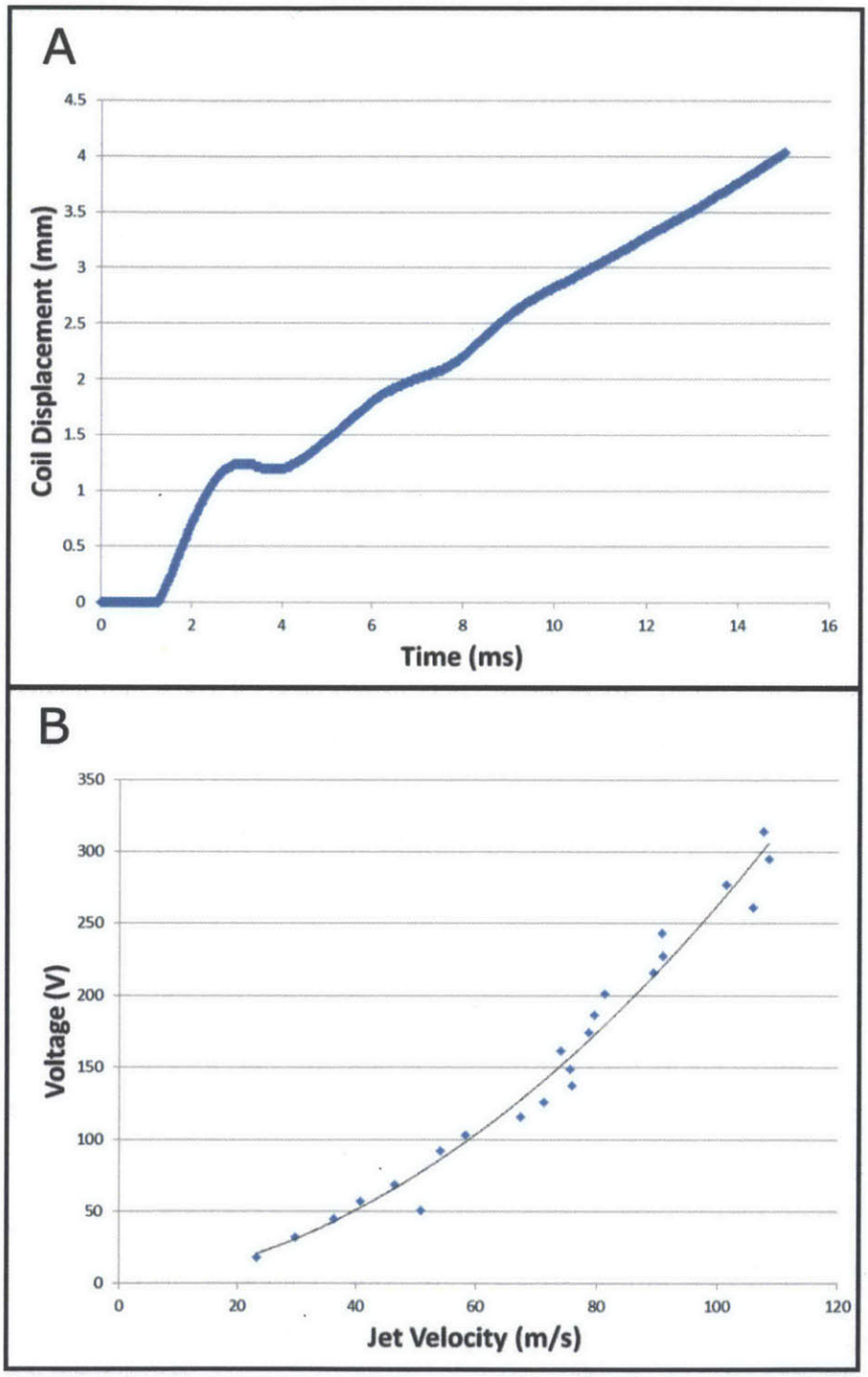

Figure 3-7: (A) Coil position in response to a step voltage input. After an initial resonance due to the piston tip, a steady-state velocity is reached. (B) When ejecting water, a quadratic relationship between voltage and steady-state velocity was found.

PhD candidate in the BioInstrumentation Lab. For any injection with certain parameters such as piercing velocity v_{jet}, following velocity v_{follow},time of piercing jet t_{jet}, and volume to be delivered, a unique position waveform was generated and communicated to the controller. The controller would calculate the velocity of the fluid at that particular point in the waveform and output a corresponding voltage. However, this method in itself would prove susceptible to changes in piston quality, and would be prone to variable steady-state errors. As a result a PID feedback controller was used in combination with the previously mentioned feed-forward controller to clean up any noises or disturbance in our signal.

Even when using the linear model derived above, choosing gains for the PID controller proved difficult. First and foremost, because of the nature of the linear encoder signal, in which the position reading is quantized, determining a derivative value from the position is computationally difficult. Any derivative controller or controller with a zero such as a lead or lag would be computationally heavy to implement. Additionally, because the system model has a free integrator, only a proportional term is necessary to eliminate steady-state error. While it would have been useful to add an integral term to our controller to improve velocity tracking of the device, this could be quite dangerous, as the term would push the steady-state phase o the open loop transmission of the system from $-90°$ to $-180°$. This confronts the user with a predicament: the integral term must be so small so that its effect is only noticeable over a large time scale, or the integral term is large enough to be noticeable, but could likely cause instability of the system. Due to this tradeoff, no additional integral term is implemented by the controller.

This resulted in a feed-forward controller in conjunction with a proportional controller (Fig. 3-8) to eliminate steady-state noise. Choosing the controller gain was quite tricky, as it had to be assumed that the damping of the system would change based on the wear, or lack of wear, of the piston tip over time. As a result, a very conservative gain was initially chosen for the controller, with the idea that the gain could slowly be incremented for a particular ampoule if the steady-state error was determined to be insufficient.

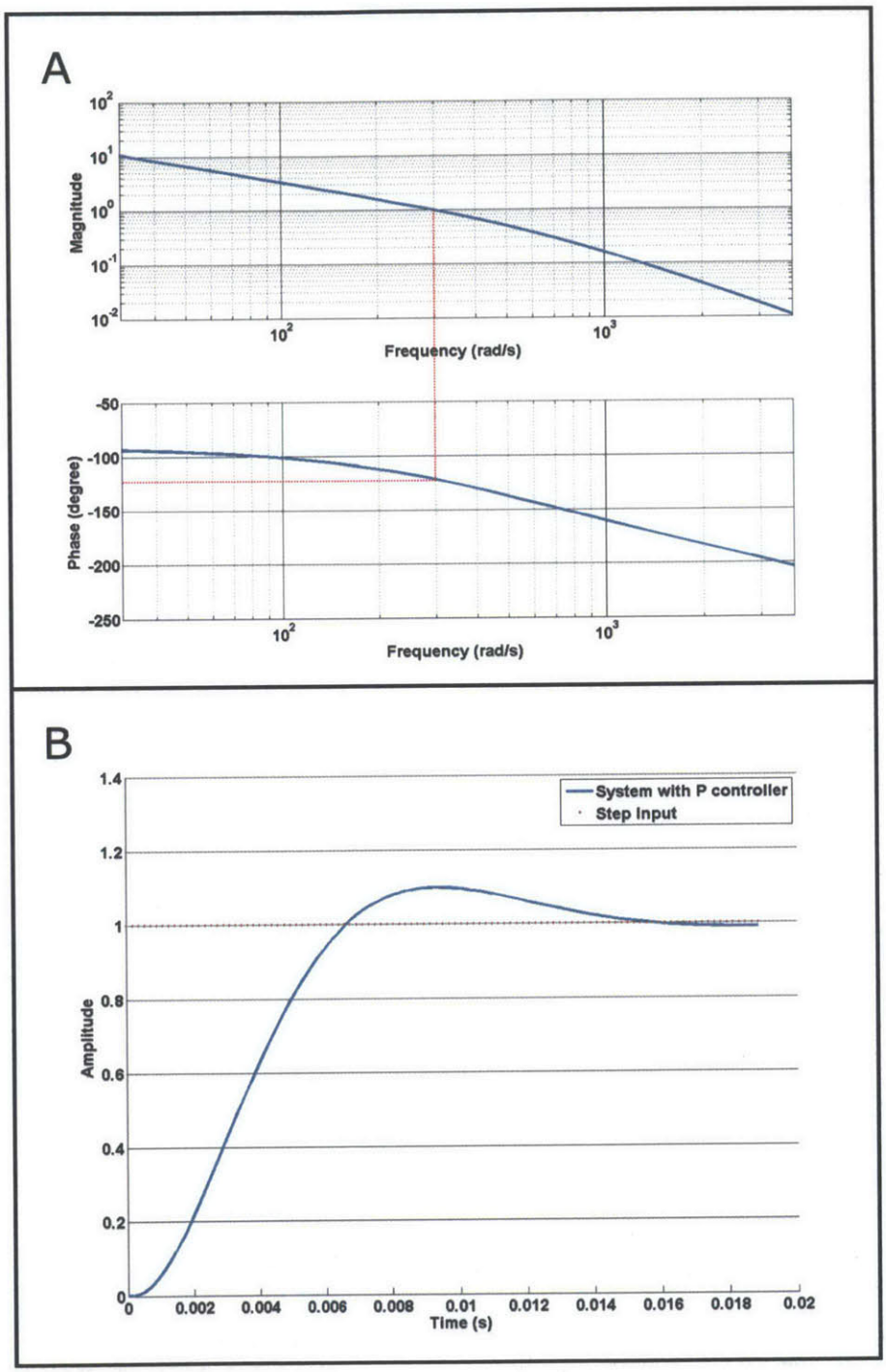

Figure 3-8: System after a P controller had been applied. (A) The resulting phase margin was 58.3° at 295 radians/s. (B) The step response resulted in a settling time of 14.2 ms with an overshoot of 9%.

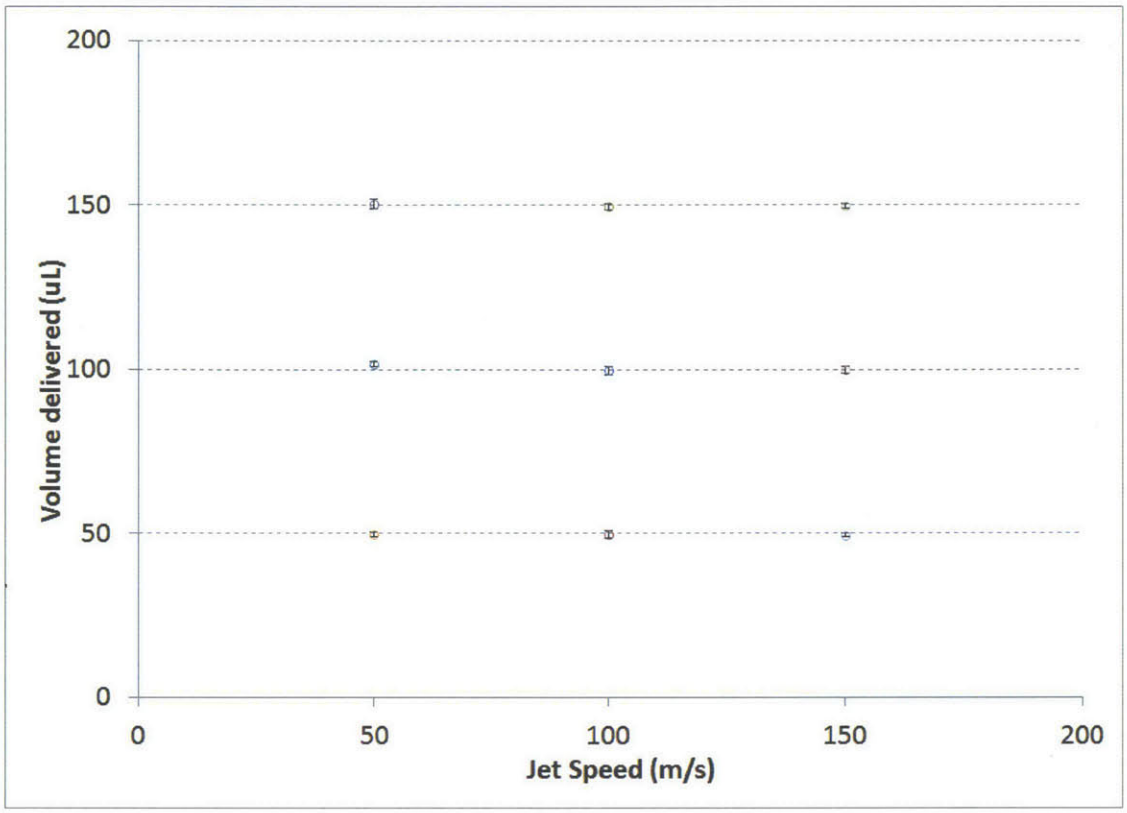

Figure 3-9: Repeatability of volume ejections. Various volumes of water were ejected at different piercing velocities. The average and standard deviations of the trials (n=10) are shown. In total, the ejections were repeatable within 1.3% of the desired volume.

3.3.4 Volume Ejections

As a final test, volume ejections were performed to determine the precision of the drug delivered when an actual waveform was applied. The profile used has three distinct parameters: an initial piercing jet velocity (v_{jet}), piercing duration (t_{jet}), and a slower following velocity (v_{follow}). Based on these three parameters, along with the desired volume, acceleration, and deceleration, a unique profile can be created for the ejection. First, ejections were performed at 1× resolution (20 µL resolution) at piercing jet velocities of 50, 100, and 150 m/s at volumes of 50, 100, 150, and 200 µL. The results of the trials are shown in Fig. 3-9.

Typical ejections showed a standard deviation of ± 1% volume delivered, comparable to that of ejections previously accomplished with a linear potentiometer. While

these results demonstrated that the linear optical encoder could be used to achieve repeatable ejections, they did not provide evidence for its use being an advantage over a linear potentiometer. Next, the system was retuned for higher gains and the encoder was set with 2× interpolation for a 10 µm resolution. Two ejection profiles were tested: a 50 µL, 50 m/s v_{jet} profile, and a 100 µL, 100 m/s v_{jet} profile. Additionally, to determine if there was any difference in delivery of the drug through the stroke of the piston, the 50 µL ejection was tested sequentially at two different starting positions, the second at the endpoint of the first to minimize the effect of piston wear. The results are shown in Table 3.3, and a sample of the ejection waveform is shown in Fig. 3-10.

Ejection Parameters	50 m/s, 50 µL Position 1	50 m/s, 50 µL Position 2	100 m/s, 100 µL
Ejected Volume (µL)	49.8 ± 0.30	48.9 ± 0.43	98.5 ± 0.25
Predicted Volume (µL)	49.6 ± 0.31	49.0 ± 0.33	99.3 ± 0.20
Error From Prediction (µL)	0.25 ± 0.21	-0.09 ± 0.17	-0.83 ± 0.25

Table 3.3: Results of volume ejections using 10 µm resolution. All ejections had a precision of 0.3 µL or better. There was a statistically significant difference in the volume delivered for the 50 µL ejections based on the initial starting position of the piston ($p \leq 0.001$, $n = 10$).

The increase in resolution and controller gain provided a rather large improvement in performance. Repeatability of all ejections was ± 0.3 µL, regardless of the volume delivered. Additionally, the difference of the delivered volume from the predicted output varied only ± 0.25 µL. Possible reasons for error between the predicted and actual volume could be the compression of the piston tip and expansion of the ampoule, both of which were unaccounted for in predicting the volume delivered. As the piston wore during ejections, the piston tip stiffness could easily change, resulting in more loss in fluid delivered. While preliminary stress-strain analysis of the ampoule showed minimal error in volume delivered due to the steady-state compression and expansion of the ampoule, it is possible that the stiffness of the ampoule varied greatly from the assumed value of 2.4 GPa.

Variability in the tip and ampoule could also explain both the statistically signif-

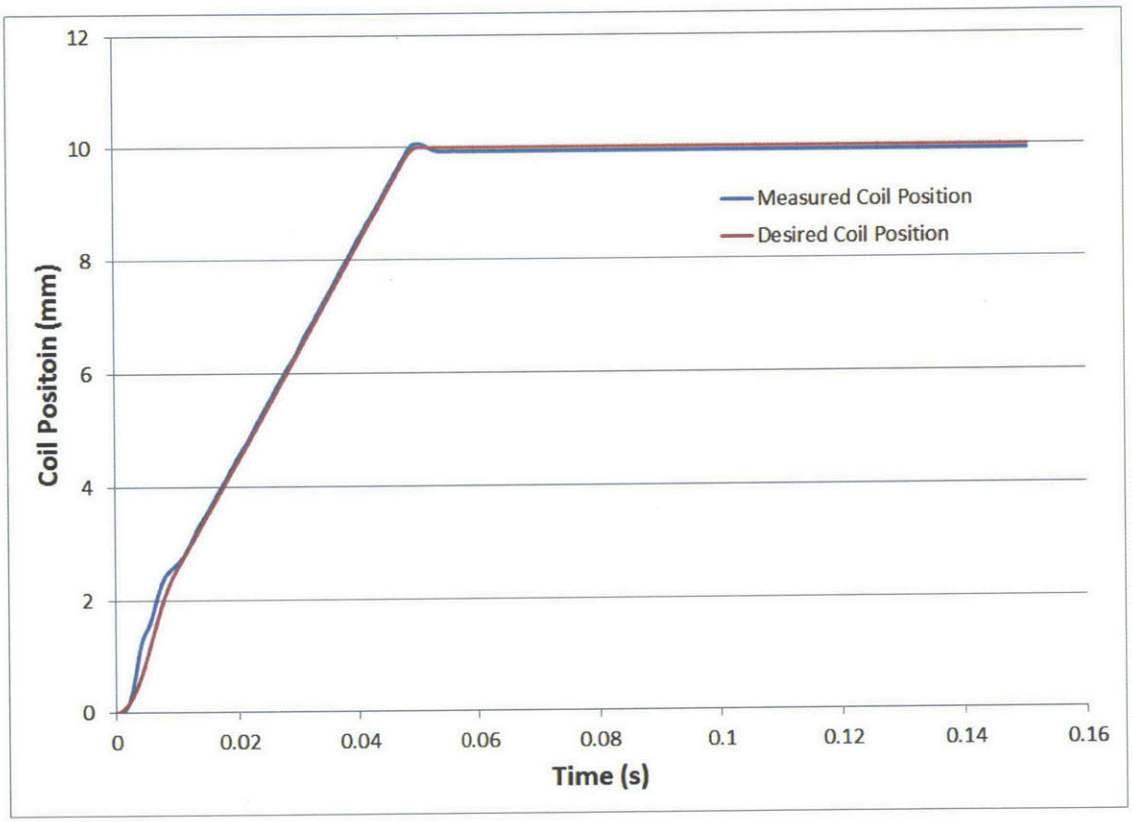

Figure 3-10: A sample trajectory waveform of a 100 µL ejection with a 100 m/s piercing jet velocity. While the coil does not follow the waveform well when accelerating, both the piercing and following velocity of the jet match the desired values.

icant differences ($p \leq 0.001$) in predicted and actual volume delivered at the two different positions when delivering 50 µL. Because the controller is based predominantly on a feed-forward relationship between the desired velocity and voltage delivered, a significant undershoot or overshoot would be caused by any change in frictional or drag components. Any variability in the inner surface of the ampoule over the length of the stroke or wear of the piston between tests could have caused additional friction and the undershoot of the desired waveform profile that was observed between the two starting positions.

3.4 Conclusion

The linear optical encoder improved the precision of volume ejection of the device. Previous ejections had a repeatability of 1% which corresponded to a 0.5 µL repeatability at 50 µL. Use of the encoder at 10 µm resolution has already produced repeatability of 0.3 µL, regardless of volume delivered. While the encoder is capable of reading at 5 µm resolution, the current hardware setup is not fast enough to capture the encoder signal when moving at injection velocities. Because the current sampling period of the compact RIO module used is only 7 µs, an ejection with 200 m/s jet velocity could be measured at 20 µm resolution, but only ejections with 50 m/s jet velocity would be able to be measured at 5 µm resolution. As a result, a faster counting encoder interface has been created for use with future microcontroller-based (ARM Cortex M4) controllers for the device. Implementation of a dedicated hardware encoder counter will allow for ejection tests to be performed at higher resolutions. Higher resolutions and sampling frequencies could also allow for additional lead-lag type or derivative controllers, provided that the encoder sampling and change occurs much faster than the control loop of the system, thereby getting rid of the quantization effect that makes calculating derivatives difficult.

While the linear encoder did improve the repeatability of the ejections, it has also shown that position resolution is not the only limitation to the precision of volume ejections. Another big source of error is the wear of the piston tip and the deformation

of both the piston tip and ampoule. A new, stiffer ampoule and piston system with less wear must be designed to further improve the repeatability of the device. Lastly, it is important to note that the linear encoder system has not yet been tested on injections. It is known that tissue load affects the dynamics of the system. Once again, a stiffer ampoule will mitigate some of these effects and will allow for higher PID gains in the control scheme, which will result for a tighter response despite the presence of these tissue loads.

Chapter 4

Vial Extraction

One essential accessory that needed to be designed and fabricated for commercialization of this device was an interface with a medicinal vial. Currently, most drugs used for needle-free injection are packaged in two different enclosures: a preloaded ampoule, or a vial of drug. While use of a preloaded ampoule is relatively straight forward, extracting drug from a vial into an empty ampoule must usually be done manually with the use of an accessory. However, the bidirectionality of the Lorentz-force actuator used in this device allows for automation of the extraction process, which is not possible for standard disposable cartridge jet injectors.

The process for drawing drug out of vial using a needle and syringe is relatively straight forward (Fig 4-1). The syringe is first drawn back to the amount of fluid desired, creating an air pocket at atmospheric pressure in the barrel of the syringe. Next, the needle tip of the syringe is inserted through a thick rubber septum into the vial. This septum is made out of self-sealing elastomer so that it may be pierced multiple times without creating a lasting puncture in the seal. Once inserted, the syringe plunger is pressed forward, expelling the air previously in the barrel into the vial. The syringe plunger is then drawn back once again, but is now filled with drug, which is at atmospheric pressure.

Extraction of drug for a needle-free injection device follows a similar procedure. However, because there is no longer any needle to pierce the septum of the vial, an adaptor must be used to interface with the medicinal vial. While each manufacturers

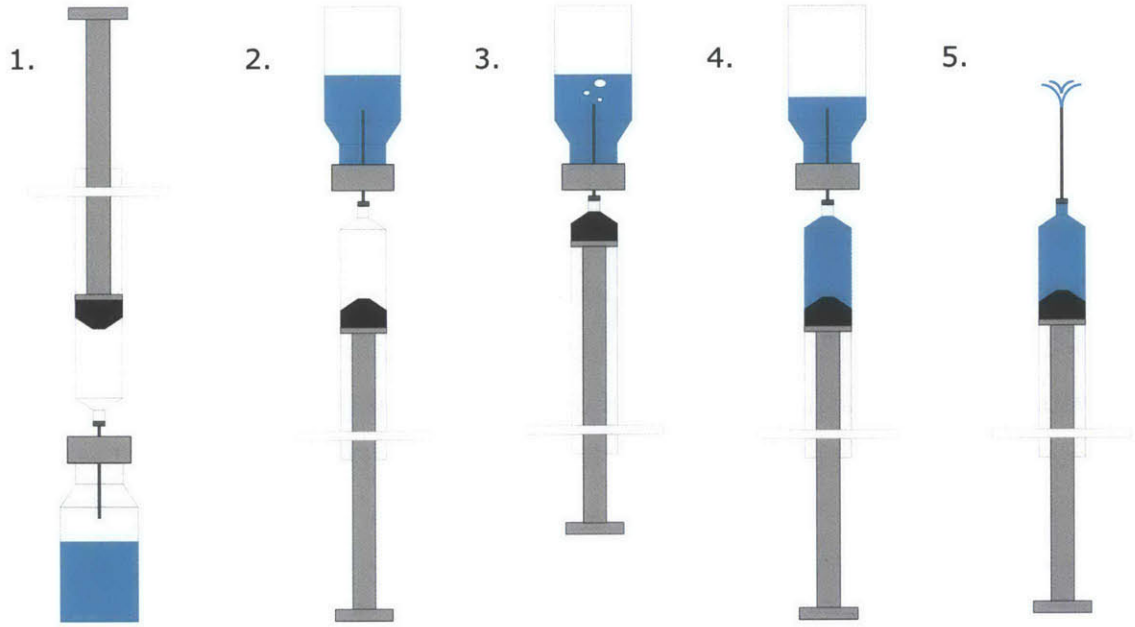

Figure 4-1: Basic procedure for extracting fluid out of a vial using a needle and syringe. (1) The syringe needle is inserted into the vial, and (2) the vial is inverted. (3) Excess air in the syringe is pushed out of the barrel and into the vial. (4) When the syringe piston is drawn back, the syringe is now filled with drug, except a small volume of dead space. (5) To get rid of this dead space, the syringe piston is pushed forward slightly (while inverted) until fluid is flowing out of the needle.

Figure 4-2: Various needle-free vial adaptors currently on the market [5] [6] [7].

design is slightly different, most share the following common factors: a flexible grasping element to attach the adaptor to the vial, a pointed cannula used to pierce the rubber septum, a sealing element that keeps pressure between the ampoule tip and the vial, a method of ensuring that the seal is not broken, and a protective cover to minimize contamination. The adaptor is permanently clasped on the vial, creating an opening through the septum to the drug inside. The ampoule is then pressed against the other side of the adaptor and an air tight seal is created between the ampoule, adaptor and vial. Next the same procedure as drug extraction with a needle is followed, with excess fluid usually expelled back into the vial or into the air once the ampoule is removed from the adaptor.

4.1 Design of a Novel Vial Adaptor

4.1.1 Overview

In the design of the vial adaptor, an attempt was made to make a simpler device that eliminated the need for a sterile cap on the device. For most vial adaptors on the market, this cap is necessary, as otherwise there would be an open channel for the outside environment to interact with the drug inside the vial. The goal was to make the sealing element of the adaptor also function as the means to ensure sterility of the vial contents. One initial design was to use a self-sealing elastomer sheet as a

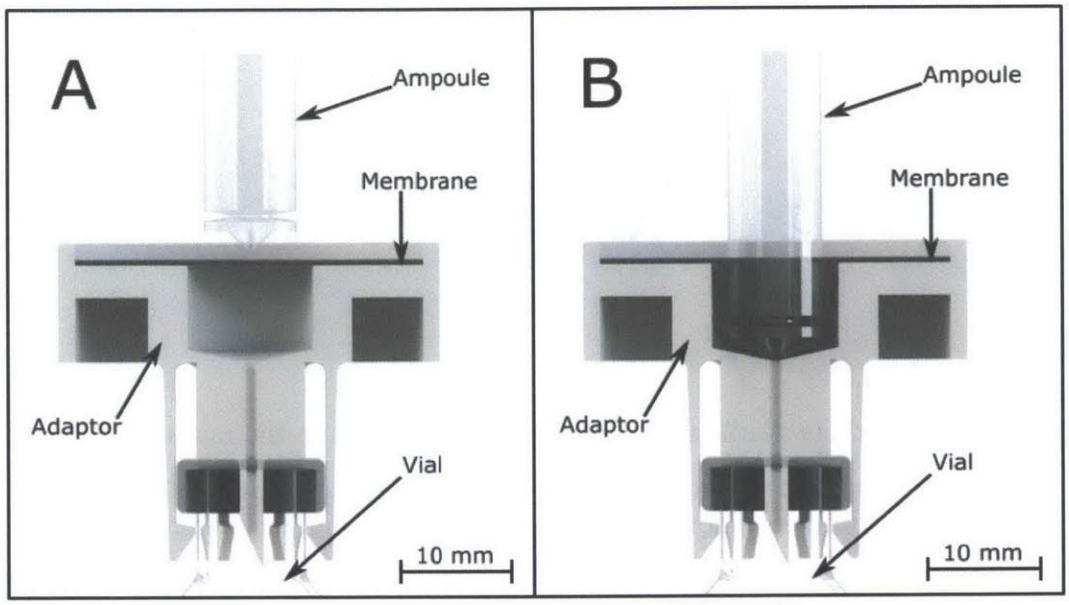

Figure 4-3: Initial concept for the sealing membrane of the adaptor. (A) Any hole in the membrane is effectively sealed when closed, but (B) this hole opens up when the membrane is stretched to allow for flow of fluid between the ampoule and vial while maintaining a seal.

cover over the adaptor. This sheet would have a tapered hole so that it was effectively sealed when flat, but would open when stretched by the ampoule towards the inner wall of the adaptor. By pressing the ampoule against this elastomer sheet, an air tight seal is also created, allowing the drawing of fluid from the now-opened hole in the elastomeric sheet into the ampoule. When the ampoule was removed, the sheet would return to its original position, providing a seal similar to the one provided by the vials own rubber septum over the vial-adaptor assembly (see Fig. 4-3).

Other than this change, the adaptor to be designed needed to meet the other common requirements a well. Snap-fitting legs were used to firmly attach the adaptor to the crimping portion of the vial, similar to previous adaptors [52] [53] [54] [55]. A plastic cannula was used to pierce through the rubber septum.

4.1.2 Snap-fit legs and Cannula Design

Most adaptors on the market use some form of flexing or snapping mechanism to attach to the necked, crimped portion of the vial, and the current adaptor was designed similarly. It was important that the fits take minimal force to attach, but require a much greater force to remove. The legs were expected to be able to deflect 4 mm without breaking, twice as far as the 2 mm needed to pass over the metal crimp. Additionally, it was desired that these legs be able to provide a guide for the piercing cannula to ensure that the cannula is inserted normal to the septum surface. To efficiently create this snap fit, a design guide was used [56] (see Fig. 4-4). While not intended as a final material, the features were designed around 3D Systems SL 60 Resin [57], which was used in rapid prototyping of the device.

The resulting design was one of six 16 mm legs whose cross sections were 15° cutouts of a circular cross section with inner diameter of 14 mm and outer diameter of 16 mm. Additionally, to improve performance, this cross section was tapered from an initial thickness of 1 mm to a final thickness of 0.5 mm. This design allowed for a theoretical maximum deflection of 4.5 mm for each leg. The tabs were given an inserting angle of 35° and a removing angle of 80°, resulting in a theoretical insertion force of 9.5 N and removal force of 75.5 N. The equations used to find these values are listed in Fig. 4-4 and are present in many snap fit design guides [56] or can be derived by hand.

The design considerations for the cannula were simple: The cannula needed to be as small in diameter as possible to not completely tear the vial septum, but still sturdy enough to not buckle and snap when inserted into the vial. While needle insertion force can be difficult to model, it is on the same order or less than that off the insertion force of the flexible legs. Depending on the coefficient of friction between the snapping legs and vial, this force can be as large as 75.5 N. If some undesired loading condition occurred in which this force was not transferred to the legs, the cannula should not buckle and snap. Modeling the cannula as a hollow cylinder with two fixed ends, an outer diameter of 2.2 mm and inner diameter of 5 mm provided

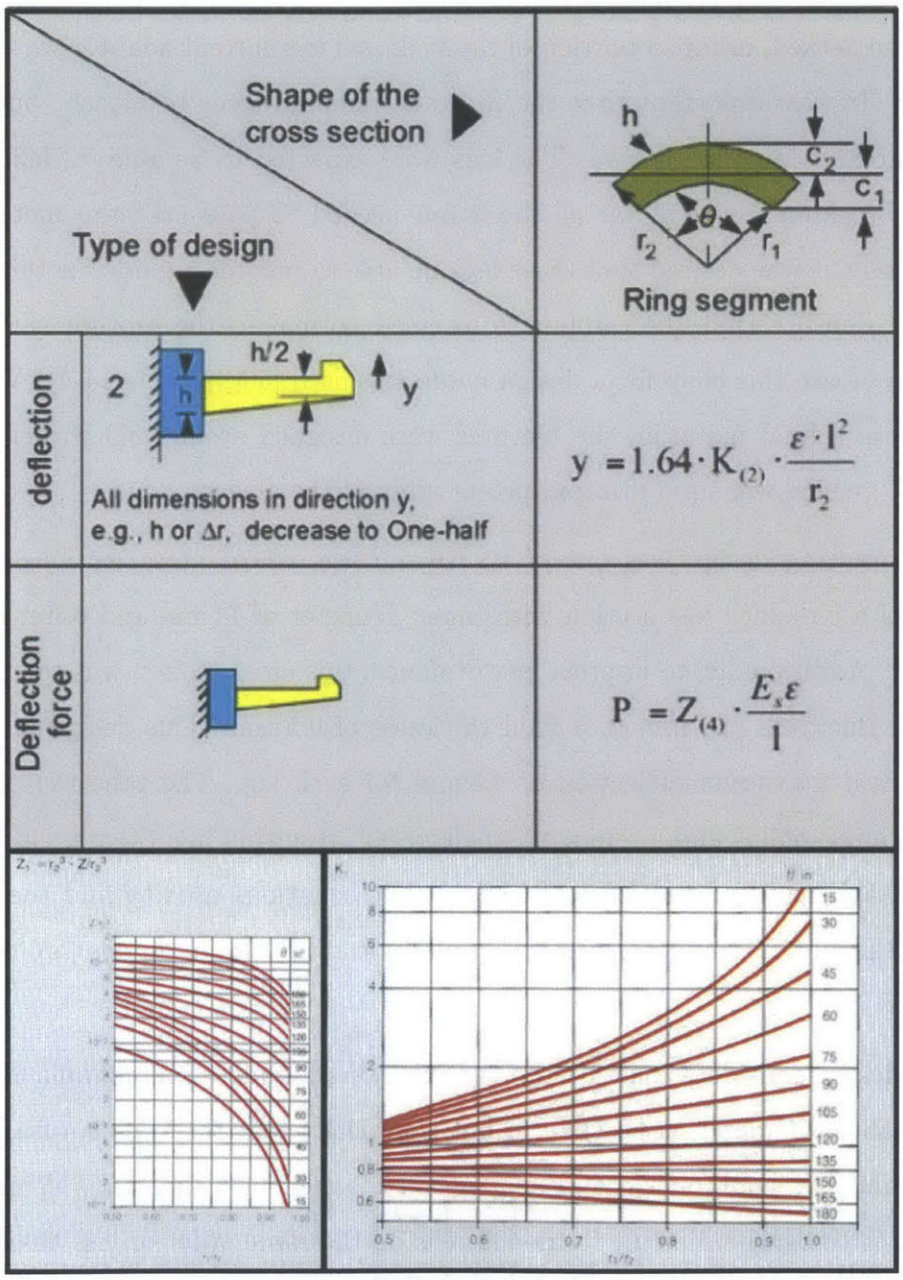

Figure 4-4: Design equations for designing snap fits taken from [56], where y is the permissible deflection, ϵ is the permissible strain in the outer fiber, E_s is the secant modulus of the material, and l is the length of the arm

resistance to buckling up to 130 N, almost twice that of the loads in the worst case loading condition. In most cases, the loads on the cannula are dominated by the insertion force of the cannula into the rubber septum. This could allow for an even thinner cannula or one with a different bevel shape to reduce these forces further.

4.1.3 Challenges in Design of the Elastomeric Seal

While a succesfull proof of concept was made, further analysis indicated that design of an acceptable final product would be challenging. To ensure that a sufficiently small hole grew large enough for the tip of the ampoule to easily fit through, the elastomeric sheet had to stretch greatly, the exact value depending on the material and thickness of the sheet. While a thicker sheet provided a better, air tight, seal against the adaptor both when the ampoule was pressed against the sheet and when the sheet was relaxed, the force needed to deform the sheet was noticeably larger. Additionally, due to the loading of this elastomeric sheet, the possible materials that could be used were very limited. The elastomers commonly used in creating pharmaceutical enclosures are halobutyls, ethylene propylenediene monomers (EPDM), and polyisoprenes [58] [59]. Of these, only butyl and EPDM provided the necessary tear and abrasion resistance to plausibly be used in such an application [60]. Butyl sheets of appropriate thickness were difficult to obtain and as a result prototypes were modeled using natural rubber or EPDM. While this design may have been plausible, it was unlikely that a compromise could be found between a low stretching force of the ampoule into the adaptor and adequate sealing characteristics for the rubber seal. To make matters worse, the ampoule had to be held at the maximum stretching force during the course of extracting fluid of the vial. Instead, a different elastomeric seal based on bistable hemispheres similar to a rubber popper has been explored.

4.1.4 Advantages to a Popper-Like Seal

The concept behind the rubber popper seal was very similar to that of a stretchable elastomeric sheet. A tapered hole would be cut in the popper so that it was sealed

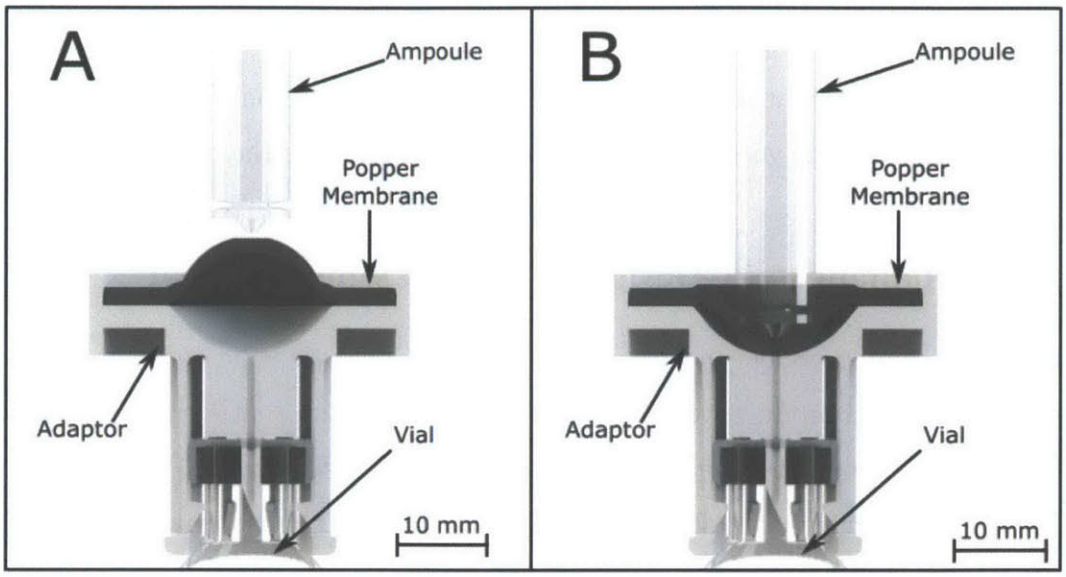

Figure 4-5: Concept using a bistable hemisphere as the seal. (A) Any hole in the membrane is effectively sealed when the popper is in its normal position, but (B) this hole opens up when the popper is inverted to allow for flow of fluid between the ampoule and vial while maintaining a seal.

when at rest, but would be opened when the popper was flipped to its inverted position (see Fig. 4-5). While force would still be needed to invert the popper, the resistance of the popper would be significantly less than the force needed to stretch a membrane. This would reduce work applied during the insertion process, and additionally give the user a clear visual cue that the ampoule had made sufficient contact with the adaptor seal. Additionally if this force was small enough, the adaptor could be held in place in hand throughout the ampoule filling process without the need of a separate mechanism such as a Luer-lock or snap fit to mantian a tight seal between the ampoule tip and adaptor.

4.1.5 Design of a Popper-Like Seal

The rubber-popper seal is based on the idea that the concave inner surface of the popper becomes convex, increasing its radius of curvature in the process and stretching any hole in the center of the popper. While the inverted surface is not necessar-

ily known, the size the hole increases is proportional to the stretching of this inner surface. Additionally the majority of the strain occurs at the center of the popper, making any hole in that area substantially larger.

Buckling of a Rubber Popper

An important design consideration was minimizing the force required to invert the popper. Much work has been done in predicting the buckling of a hemisphere, and these equations have been used as a model for design of rubber poppers in the past [61] [62]. As outlined by SU Gailev [63] a basic equation using linear theory presented by R Zoelly [64] and L. S. Leibenson [65] for the loading of a thin elastic spherical shell is given below:

$$P = \frac{2Eh^2}{\sqrt{3(1-v^2)}R^2}, \tag{4.1}$$

where P is the external pressure, E is the young's modulus, h is the shell thickness, v is the Poisson's ratio, and R is the radius of the shell. v is assumed to be 0.499 for an elastomeric material, and the Young's modulus is estimated from the elastomer hardness using:

$$\log E = 0.0235S - 0.6403, \tag{4.2}$$

where S = Shore A durometer hardness [66]. However, this model can grossly overestimate the buckling force required to buckle a shell. A corrected formula which accounts for geometric nonlinearities of the shell was proposed in 1950 by Mushtary and Syrkin [67]:

$$P = \frac{0.36Eh^2}{\sqrt{(1-v^2)}R^2}. \tag{4.3}$$

Additionally, because the seal design needs indent for the ampoule tip to fit into, a model that takes into account this initial imperfection must be used. It has been shown by SU Gailev [63] that the buckling of a hemisphere with imperfections can be

described using a regression equation of the form:

$$\sigma = 0.11222 - 0.017X_1 - 0.01985X_2 + 0.00466X_1^2 - 0.00283X_2^2$$
$$+ 0.0065X_1X_2 - 0.0025X_1^2X_2 - 0.000499X_1X_2^2$$

where:

$$X_1 = \frac{R}{h}, \tag{4.4}$$

$$X_2 = \frac{W_0}{R}, \tag{4.5}$$

$$P = \sigma\frac{Eh^2}{R^2}, \tag{4.6}$$

where W_0 is the diameter of the imperfection.

A significant limitation of these equations is that they have been validated for metal shells and are not necessarily accurate for elastomers, due to the hyperelasticity of elastomers. Additionally, our shell thickness will be much thicker than the usual thin wall assumptions. Lastly, the exact magnitude of the force also depends on the manufacturing imperfections in the shell. To get at true idea of the magnitudes being generated, the design had to be iterated and forces measured experimentally.

Monstability, Bistability, and Pseudo-Bistability

Key work has been done to characterize the stability of hemispheres [68] [69] [70] [71]. In summary, the stability of a dome can be determined by a single geometric parameter λ:

$$\lambda = (12(1-v^2))^{\frac{1}{4}}(\frac{R}{h}\alpha)^{\frac{1}{2}}, \tag{4.7}$$

where α is half of the angle (in radians) spanned by the dome, meaning a complete hemisphere would have a α value of $\pi/2$.

This parameter has been validated for elastomeric materials as a proper estimate for stability [68]. Essentially, for any $\lambda < \lambda_0$ the specific dome is *monostable*, meaning

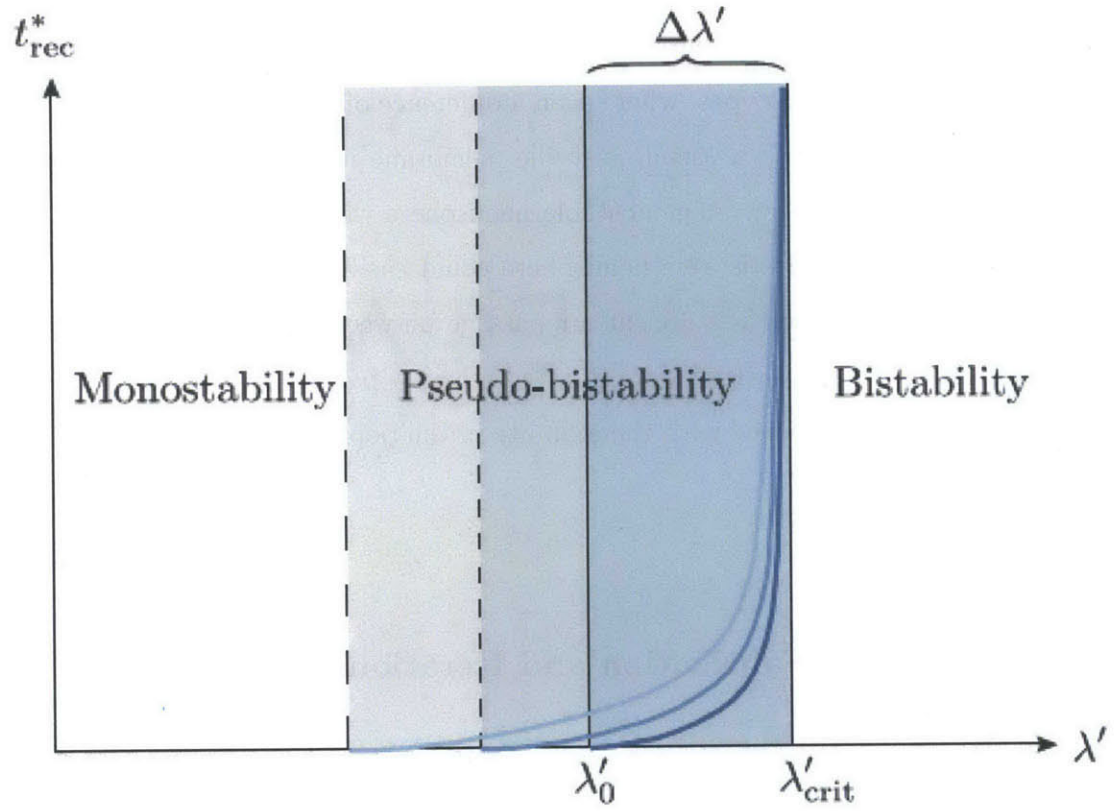

Figure 4-6: Stability of a hemisphere is defined as the time needed for it to recover to its original shape. Monostable hemispheres return to form immediately, while bistable hemispheres will stay inverted indefinitely. Pseudo-bistability is achieved when there is a finite, non-zero recovery time. λ_0 and λ_{crit} are defined as the boundary λ values for which this condition is met. Figure reproduced from [69]

that it will immediately snap back if inverted, while for any $\lambda > \lambda_{crit}$ the specific dome is *bistable*, meaning that it will stay in its inverted position indefinitely. Moreover, if $\lambda_0 < \lambda < \lambda_{crit}$, the sphere is *pseudo-bistable*, meaning that it will rest in its inverted position for a period of time before "snapping back." This last region of stability would be ideal for the current application, as it would require the least amount of force to keep a seal against the adaptor, while also not requiring any actuation to "snap back" the membrane. However, this parameter is very sensitive to manufacturing tolerances of the prototypes, where even a difference of thickness of 0.1 mm in the shell thickness would push a pseudo-bistable membrane into the bistable or monostable regime for the design. A monostable hemisphere was considered preferable to a bistable hemisphere: a bistable hemisphere could easily get stuck in its inverted position, which would provide a clear air passage between the vial and outside atmosphere. As different designs were iterated, their λ parameter was calculated to observe their correspondence with the stability of the popper.

4.1.6 Protoype Fabrication and Iteration

Material Selection

A 50 durometer Smooth-On polyurethane rubber [72] was selected for prototyping. While this material is neither self-sealing nor viable for pharmaceutical use, it was used as a placeholder for a halobutyl material of similar hardness. While the polyurethane design is not expected to translate perfectly to a halobutyl model, it provides a cost efficient way to iterate many times until a final design has been reached. Though the self-sealing, gas permeability, and wear properties of a halobutyl are expected to be different from the polyurethane rubber, it is expected that the buckling force for a particular geometry between the two materials would be within the same order of magnitude, as related by equation 4.2.

Mold Creation and Molding Process

To allow for relatively quick iteration, molds were rapid prototyped in Accura 60 material [57] on a 3D Systems Viper si2 system [73]. Channels were constructed in the design to allow for out flow of excess material during the molding process, and each mold was treated with release agent prior to use. Once the Smooth-On elastomer compound had been mixed with the curing compound, the mixture was degassed and poured into the bottom portion of the mold. The top part of the mold was then pressed down onto the bottom, with approximately 10 N of force applied to prevent unwanted expansion of the mold due to the volume elasticity of the curing compound. After a cure time of 16 hours, the rubber popper was removed and allowed to further cure and dry in an oven at 65 °C for 4 hours.

Design and Assembly

Because these popper seals needed to be adhered onto the adaptor device, a method for providing a continuous force during adhesion was desired to ensure an air-tight seal between the elastomer and adaptor. N52 neodymium ring magnets with a 19.05 mm inner diameter and 31.75 mm outer diameter were used to provide the clamping force, and Loctite 4014 [74], a medical grade adhesive, was used to join the two together. This process provided a constraint on the maximum radius of the seals: the hemisphere and all surrounding features had to fit within the 19.05 mm diameter hole of the magnet to ensure that they were not pinched during the adhesion process. In reality, this limit was set to 18 mm.

Ribs around Design

It is important to note that each popper was designed as a portion of a hemisphere on top of two conical ribs. The reason for these ribs is to allow the edges of the hemisphere portion of the popper to be closer to the sliding hinge boundary conditions as they are assumed to be in both equations for buckling and stability. Previous work on rubber poppers has shown that constraining these ends greatly affect the critical

buckling force and stability of the popper [61], and the use of these conical ribs allows for adhesion of the elastomeric popper to the adaptor without any worry regarding constraints on the edges. The angle of these conical edges was derived from previous popper patents [75] that used these conical edges as the primary flexing element in their popper. However, while the ribs in the popper-seal design are also designed to flex, they are by no means the primary flexing mechanism in the seal. When iterating designs, the lengths of these ribs were determined to be the excess lengths between the diameter of the hemisphere and the maximum possible diameter of the popper and surrounding features (18 mm).

Results of Popper Iterations

Radius (mm)	Thickness (mm)	Half-Angle (deg)	λ calculated	Stability Type	Expected Load via Gailev (N)	Expected Load via Mushtary (N)	Measured Buckling Load (N)
7.5	1	50	4.43	Pseudo-Bistable	0.69	1.27	0.69
7.5	2	50	3.13	Monostable	1.31	5.08	3.89
10.875	1	40	4.77	Pseudo-Bistable	0.65	0.60	1.26
10.875	2	40	3.38	Monostable	0.87	2.42	6.84
8.13	1	67.3	5.35	Bistable	0.60	1.08	0.71
8.13	2	67.3	3.79	Monostable	1.11	1.11	3.73

Table 4.1: Experimental results regarding buckling load and stability of various popper iterations versus expected values. The iteration shaded in gray was deemed acceptable for the design.

For most of the cases, the maximum load applied during the buckling process fell within the two values predicted by Mushtary and Gailev (see Table 4.1). When the half-angle of the hemisphere approached 40°, neither model was accurate, as the shape of the popper deviated too much from the hemisphere assumed in the model. The buckling forces predicted by Mushtary were more accurate, as it took the Poisson's ratio into factor, while Gailevs regression assumed the material was metallic. The consistent undershoot of the expected value could be attributed to defects in the manufacturing process, causing small bubbles or imperfections in the polymer, and the fact that the poppers tested were not full hemispheres.

While the critical λ values did not match those in the literature for predicting bistability, the general trend, that an increasing λ value implies increasing bistability was still present. The transition regime for bistability occurred in the range of λ values between 4.4 - 4.8. The final chosen design (shaded in gray in Table 4.1) approached this critical value but did not cross it. This final design was chosen because it had a minimum buckling force, was close to being pseudo-bistable, and was thick enough to plausibly seal the vial.

4.1.7 Hole Creation

Initially, holes were created in the polyurethane poppers by stretching the material and using a 22 gauge needle to puncture the center. While this proved effective in creating an opening for fluid to flow through, it did not provide an accurate representation of the tapered cut desired. Additionally, the ability of the elastomer to effectively seal the hole from the needle could not be gauged in the polyurethane prototype: the hole created by the needle was always visibly present. Next, holes of various diameters were created in the polyurethane poppers using a laser cutter, and their ability to let fluid flow when inverted, but not in its normal position, were assessed to determine if the hole were small enough to act as a seal. The results are shown in Table 4.2.

Top layer hole diameter (µm)	Bottom layer hole diameter(µm)	Bottom layer inverted hole diameter (µm)	Alows fluid to pass when inverted	Prevents fluid from passing normally
364.8	182.4	638.4	Y	N
364.8	91.2	456.0	Y	N
310.8	0	218.9	N	Y
364.8	145.9	456.0	Y	N
328.3	36.5	273.6	Y	Y
328.3	0	364.8	Y	Y

Table 4.2: Measurements of the diameter of the conical hole created in the popper for the top and bottom side in the normal position, and the bottom side when the popper is inverted. The iterations shaded in gray were deemed acceptable for the design.

A close to ideal hole size for the polyurethane was found between 0 to 36.5 µm. However, it must be noted that at higher pressures the hole on the bottom side of the popper would open up even in its normally closed position. A more prudent combination may consist of a tapered hole until a critical thickness, after which a slit is created using a needle or pin. Unfortunately, this ideal hole size will be dependent on the self-sealing properties of the final elastomer, ideally a halobutyl, that is used, and cannot be accurately estimated by the current polyurethane iterations.

4.1.8 Final Design

The final design for the adaptor is shwon in Fig. 4-8: 16 mm legs were used for the snap fits with an insertion angle of 35° and removal angle of 80°. A 2.2 mm cannula was used with a 66° bevel. The final insertion force of the adaptor was found to be 14.5 N . The interface to which the rubber popper was to abut was a 9 mm diameter hemispherical cavity. The popper seal consisted of an 8 mm diameter hemisphere with two 0.5 mm ribs. Finally, the design was covered with a protective ring to prevent accidental contact with the cannula or snapping of the flexible legs during handling of the device. The device was tested succesfully and enabled transfer of fluid from a vial into an Injex [5] ampoule with a nozzle orifice diameter of 193 µm.

Much more work remains to be done. A major component of the design, the expansion of the sealed hole must be examined closely with a halobutyl prototype. While a halobutyl compound that complies with the necessary requirements of our device and of those required by pharmaceutical enclosures has been decided on, prototypes have not yet been manufactured. Additionally, while the popper adaptor has a relatively low buckling force, it would still be ideal to have a guiding and clamping system for the user to guide the ampoule into the adaptor.

4.2 Bubble Expulsion

Once fluid has been drawn into the ampoule, any remnant air bubbles in the ampoule due to dead space in the adaptor must be discarded. This problem is common to all

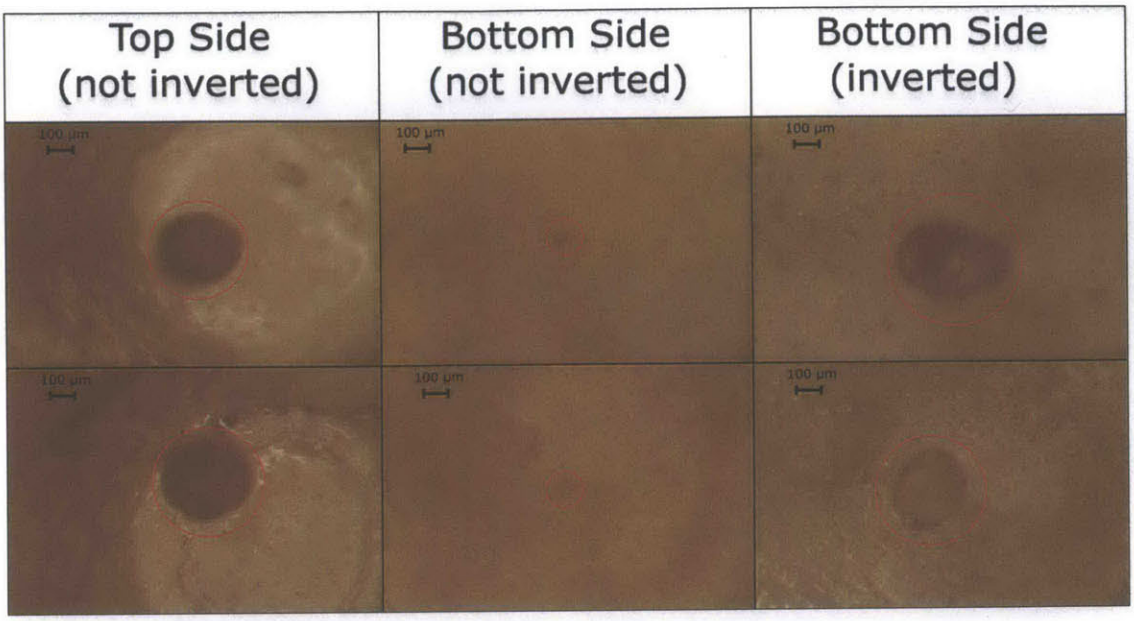

Figure 4-7: 6.6× magnification of the holes created in the polyurethane via laser cutter. Holes on the top and bottom sides in the popper's natural position and the bottom side in its inverted position are shown. Holes shown are the successfully peforming holes shaded in gray in Table 4.2.

procedures in which fluid is extracted from a vial, be it with a needle or with a needle-free device. When drug has been extracted with a syringe, the common practice is to push the plunger slightly forward, until fluid begins to flow out of the needle. In needle-free injectors on the market today, the plunger is fired forward a certain amount to expel air as well some quantity of fluid. While both these processes are effective, the user has no definitive means to determine the exact point at which all the air has been evacuated. This results in unnecessary loss of fluid, as either the device or the user must overcompensate to ensure that all air is expelled out of the chamber. A second consequence is that additional time must be placed to ensure there are no more bubbles are present in the device. This involves tapping the syringe of ampoule barrel to collect all bubbles at the tip of the ampoule, pushing the plunger a set amount forward until fluid is ejected, and then visually inspecting the ampoule afterwards to ensure that all bubbles have been expelled.

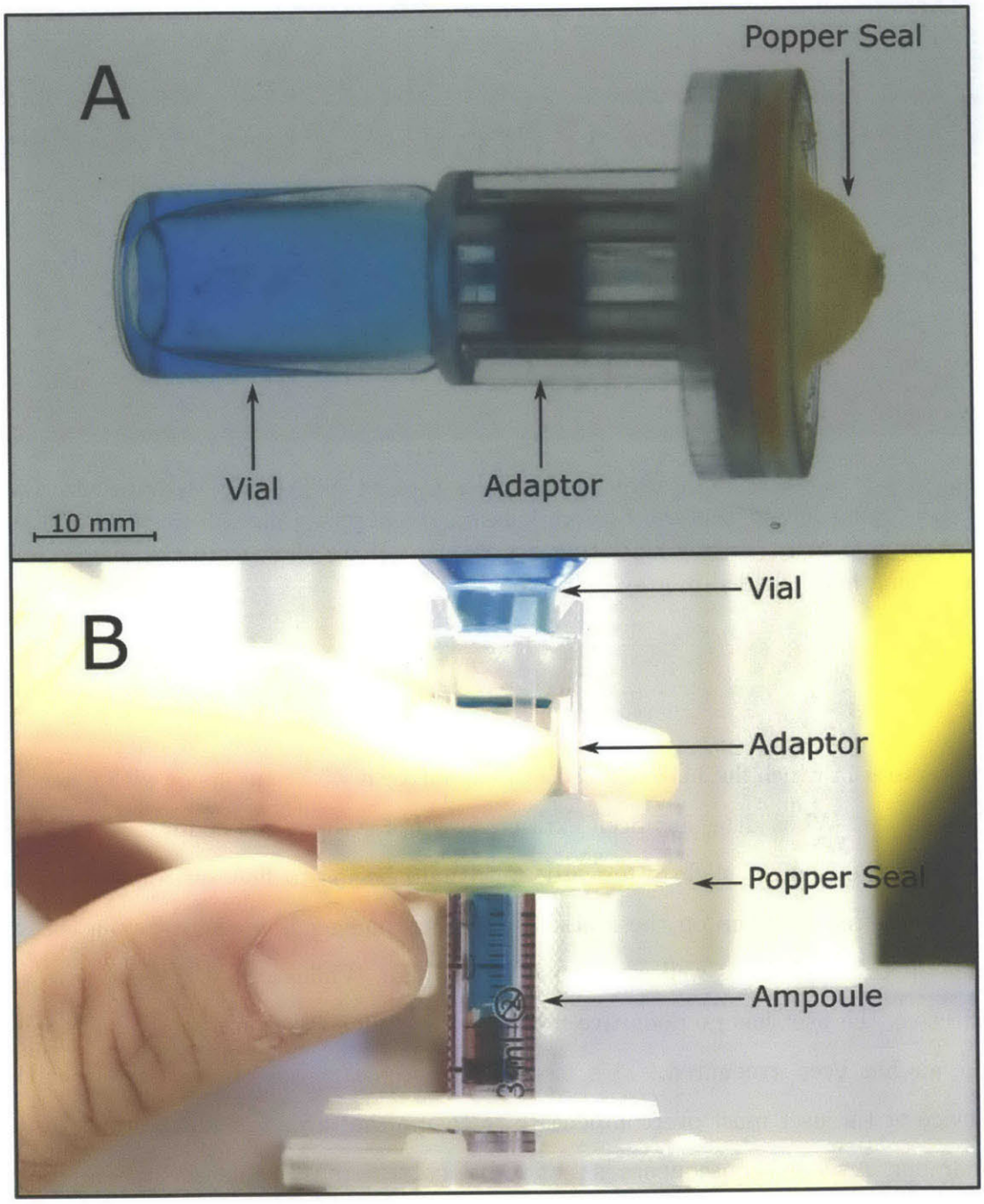

Figure 4-8: (A) Picture of the final design attached to a vial. (B) The popper design was effective in drawing fluid from a vial.

4.2.1 Automatic Bubble Expulsion

The high position resolution of the jet injector can be used to automatically determine when air is present as a bubble at the tip of the ampoule or not. This is because of the difference in the volume elasticity of air versus water. Water resists the force of the plunger more than air does, and as a consequence is harder to expel out of the ampoule than air is. As a result, as the piston plunger is pushed forward, a noticeable increase in resistance to expulsion is expected. To test this hypothesis, a bubble was created in the ampoule by drawing up fluid, ejecting so that a certain amount of fluid was left, and then retracting the ampoule an arbitrary amount. This created a bubble at the tip of the ampoule so that when the piston was pushed forward the air bubble would be the first medium ejected from the ampoule. Next, a 100 Hz square wave with a 6 N amplitude and 0.3 N offset was used to slowly vibrate the piston tip toward the end of the ampoule. The vibration of the piston provided two functions. First, the perturbing of the fluid would encorage aggregation of small bubbles to the tip of the ampoule. Secondly, the vibration allowed the piston to move down slowly without being stopped by friction. As seen in Fig. 4-9, there was a noticeable elbow in the path of the piston at the estimated position where all air had been expelled, in which the average forward velocity of the piston markedly decreased. Plotting these velocities showed that the average piston velocity linearly decreases until it hits the expected position at which all air had been expelled, where its slope changes dramatically. This is to be expected: as more and more air leaves the ampoule, the impedance of the air-water mixture to the piston force approaches the impedance of just water, which increases the resistance to the forward motion of the piston.

This effect can be examined further when looking at the distance between the local maxima and minima of the vibrations of the piston as it moves forward (see Fig. 4-10). When an air bubble is present, the forward displacement of the piston is very high, and the backward displacement of the piston is very low. When only water is present, the forward displacement of the piston decreases and the backward displacement of the piston increases, resulting in a lower forward velocity. While the

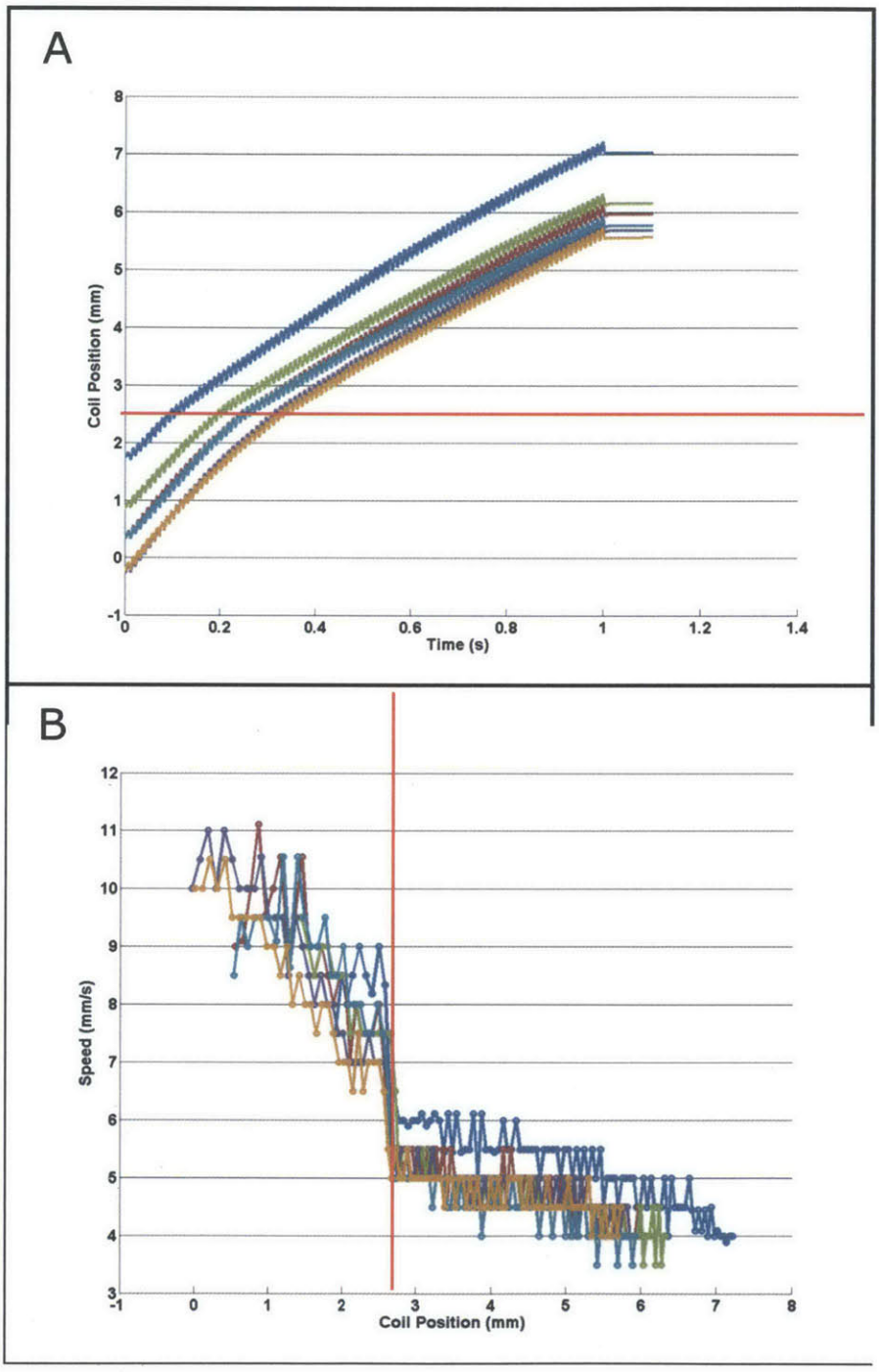

Figure 4-9: The piston is oscillated with a 6 N square wave and is slowly moved toward the tip. (A) As all the air is expelled from the piston (red line), there is a distinct elbow in the plot of coil position for the given input. (B) The average velocity of the coil decreases linearly and then jumps to a new value once the air is expelled from the piston (red line).

magnitude of forward displacement mirrors the graph of forward velocity in that it decreases fairly linearly until the point where all the air is expected to be expelled from the ampoule, the graph of the magnitude of backward displacement of the piston is interesting in that a more distinct step is present at the point where all the air is expelled from the piston. This effect could be due to volume elasticity, the presence of an air-water-ampoule interface, or both. Volume elasticity explains that water has a noticeable push-back to the piston while air does not, meaning that it will aid in pushing the piston backwards, while air will not. The presence of an air-water-ampoule interface could also make it energetically difficult to draw back the piston, as pulling backwards would cause stretching of the meniscus backwards.

Either way, because the change in magnitude of the piston's backward displacement was found to be very repeatable and exhibited a distinct change when all air was expelled, it was used as the check in the creation of an automatic bubble expulsion program to determine when to stop the piston. The program vibrated the piston tip at 100 Hz at 6 N and slowly moved it forward with a 0.3 N offset. The magnitude of the backward displacement was recorded and when this magnitude was greater than an experimentally determined threshold, the piston was immediately stopped.

Experiments were conducted with bubble sizes of approximately 5 and 16 µL. In all cases, a small volume of fluid was ejected, ensuring that the piston did not prematurely stop before all the air had been removed. Initial tests of 16 µL had a fluid loss of 1.58 ± 1.07 µL, which was rather high. A lower, less conservative threshold was then used for the 5 µL bubble expulsions, and the fluid loss was 0.78 ± 0.56 µL.

4.2.2 Further Work

While it is encouraging that this automated methods is effective in removing small bubbles with minimal fluid loss, this technique can be refined further. The same basic principles could be observed if the piston was put in position control, and the voltage necessary to drive the coil was measured. However, this is subject to the same problems encountered in the previous chapter: current control schemes make it difficult to raise the gains of the controller enough to adequately account for

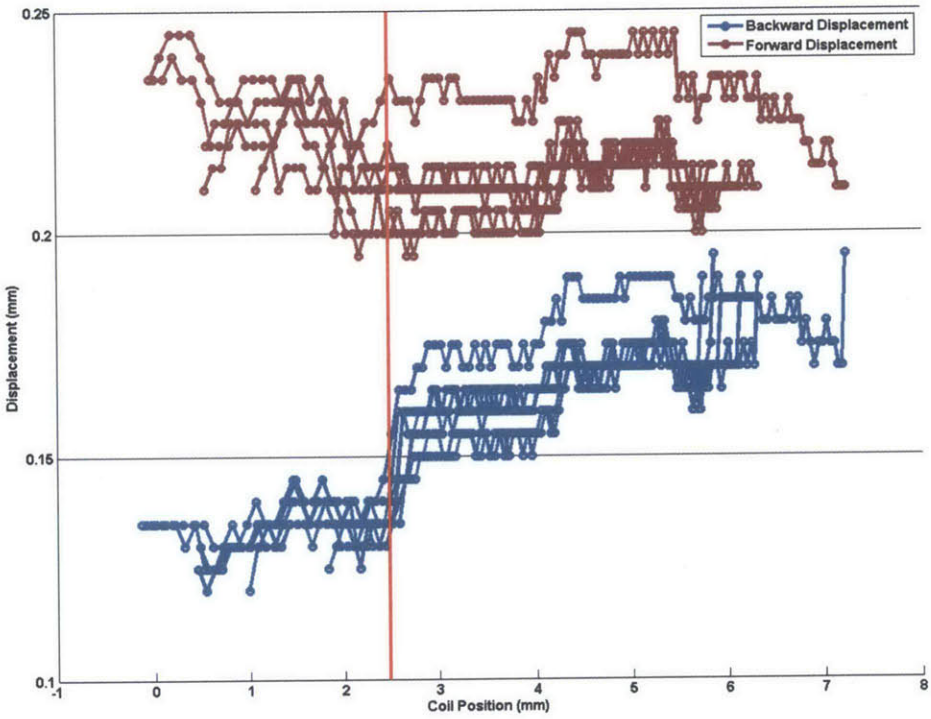

Figure 4-10: When the air is expelled out of the ampoule (red line), only water is left inside. The forward displacement of the piston decreases, while the backward displacement of the piston increases.

disturbances or to allow for minute changes in position. Another important hurdle is correctly perturbing the piston tip when the ampoule is faced upwards, so that any bubble not at the tip of the ampoule will float to the top. While this concept is similar to those often used in practice, it was difficult to implement with the current ampoule setup. One solution was to draw fluid upside down from the beginning, so that bubbles will automatically aggregate at the top as the piston is pulled backwards. A more permanent solution would be to cover the inner surface of the ampoule with a hydrophilic coating to aid in aggregation of air bubbles in water based media [76].

4.3 Conclusion

A vial adaptor has been prototyped that allows for extraction of fluid from a medicinal vial using the needle free injector. This vial adaptor uses a novel, bistable membrane as a seal, needing minimal force to be engaged. This prototype must still be refined for commercial production. Along with this adaptor, an automated bubble expulsion program was created to remove any air that collects in the ampoule during the extraction process. The automated program has been shown to expell air from the vial with minimal (0.56 µL) fluid loss.

Chapter 5

Conclusion

The aims of this work was to improve various aspects of the current needle-free injection device that would move it closer to a device readay for commercialization for individual human use. These improvements included the implementation of additional sensors, including a Hall effect sensor and infrared thermopile which provide quality and safety checks. Flexible elements are used to reduce mechanical fatigue and extra drag from the moving wires in the previous design. Position sensing was improved over the linear potentiometer to a non-contact method by implementing a low cost linear optical encoder system. This encoder provided increased position resolution, and this improved precison of volume delivered and allowed for a new automated bubble expulsion method. Lastly, a prototype for a novel vial adaptor for use with the needle free injector has been fabricated.

The immediate future goals following this thesis are clear: moving the current LabVIEW based controller to a microcontroller will aid both in portability of the device, as well as allow for increased resolution in piston position during injections. A stiffer, more repeatable ampoule is desired to further improve the precision of the device as well. Lastly, the current vial adaptor prototype must be fabricated in butyl and reviewed critically with respect to design for manufacturing.

Bibliography

[1] M. L. Lockhart, "Hypodermic injector," June 22 1943. US Patent 2,322,244.

[2] S. Mitragotri, "Current status and future prospects of needle-free liquid jet injectors," *Nat. Rev. Drug Discov.*, pp. 543–548, June 2006.

[3] Bioject Medical Technologies, Inc., Lake Forest, CA. `http://www.bioject.com/`.

[4] Zocgcnix, Inc., San Diego, CA. `http://www.zogenix.com/`.

[5] Injex Pharma Ltd., Miama, FL. `www.injex.com`.

[6] Antares Pharma, Inc., Minneapolis, MN. `http://www.mediject.com/`.

[7] PharmaJet , Golden, CO. `http://www.pharmajet.com//`.

[8] Crossject Medical Technology, Chenove, France. `http://http://www.crossject.com/`.

[9] Valeritas, Inc., Bridgewater, NJ. `https://www.valeritas.com/`.

[10] N. Inoue, H. Todo, D. Iidaka, Y. Tokudome, F. Hashimoto, T. Kishino, and K. Sugibayashi, "Possibility and effectiveness of drug delivery to skin by needle-free injector," *International Journal of Pharmaceutics*, vol. 391, no. 12, pp. 65 – 72, 2010.

[11] C. Brearley, A. Priestley, J. Leighton-Scott, and M. Christen, "Pharmacokinetics of recombinant human growth hormone administered by cool.clicktm 2, a new needle-free device, compared with subcutaneous administration using a conventional syringe and needle," *BMC Clinical Pharmacology*, vol. 7, no. 1, p. 10, 2007.

[12] N. Jimenez, H. Bradford, K. D. Seidel, M. Sousa, and A. M. Lynn, "A comparison of a needle-free injection system for local anesthesia versus emla for intravenous catheter insertion in the pediatric patient," *Anesthesia & Analgesia*, vol. 102, no. 2, pp. 411–414, 2006.

[13] W. Walther, U. Stein, I. Fichtner, and P. Schlag, "Low-volume jet injection for efficient nonviral in vivo gene transfer," *Molecular Biotechnology*, vol. 28, no. 2, pp. 121–128, 2004.

[14] A. Taberner, N. Ball, N. Hogan, and I. Hunter, "A portable needle-free jet injector based on a custom high power-density voice-coil actuator," in *Engineering in Medicine and Biology Society, 2006. EMBS '06. 28th Annual International Conference of the IEEE*, pp. 5001–5004, 2006.

[15] A. Taberner, N. C. Hogan, and I. W. Hunter, "Needle-free jet injection using real-time controlled linear lorentz-force actuators," *Medical Engineering & Physics*, vol. 34, no. 9, pp. 1228 – 1235, 2012.

[16] D. Wendell, B. Hemond, N. Hogan, A. Taberner, and I. Hunter, "The effect of jet parameters on jet injection," in *Engineering in Medicine and Biology Society, 2006. EMBS '06. 28th Annual International Conference of the IEEE*, pp. 5005–5008, 2006.

[17] N. Hogan, B. Hemond, D. Wendell, A. Taberner, and I. Hunter, "Delivery of active collagenase to skin using a lorentz-force actuated needle-free injector," in *Engineering in Medicine and Biology Society, 2006. EMBS '06. 28th Annual International Conference of the IEEE*, pp. 5611–5616, 2006.

[18] B. Hemond, D. Wendell, N. Hogan, A. Taberner, and I. Hunter, "A lorentz-force actuated autoloading needle-free injector," in *Engineering in Medicine and Biology Society, 2006. EMBS '06. 28th Annual International Conference of the IEEE*, pp. 679–682, 2006.

[19] J. R. Schramm-Baxter and S. Mitragotri, "Investigations of needle-free jet injections," in *Engineering in Medicine and Biology Society, 2004. IEMBS '04. 26th Annual International Conference of the IEEE*, vol. 2, pp. 3543–3546, 2004.

[20] J. C. Stachowiak, T. H. Li, A. Arora, S. Mitragotri, and D. A. Fletcher, "Dynamic control of needle-free jet injection," *Journal of Controlled Release*, vol. 135, no. 2, pp. 104 – 112, 2009.

[21] E. E. Kis, G. Winter, and J. Myschik, "Devices for intradermal vaccination," *Vaccine*, vol. 30, no. 3, pp. 523 – 538, 2012.

[22] B. D. Hemond, "A lorentz-force actuated controllable needle-free drug delivery system," Master's thesis, Massachusetts Institute of Technology. Dept. of Electrical Engineering and Computer Science., 2006.

[23] N. B. Ball, "An optimized linear lorentz-force actuator for biorobotics and needle-free injection," Master's thesis, Massachusetts Institute of Technology. Dept. of Mechanical Engineering, 2007.

[24] National Instruments, Austin, TX. `www.ni.com`.

[25] Alps Electric, Sensors Linear Type RDC10 Series.

[26] Mazak Corporation, Florence, KY. http://www.mazakusa.com/.

[27] Avago Technologies, 3 Channel Reflective Incremental Encoders, AV02-2790EN, Sept. 2011.

[28] Allegro MicroSystems Inc., Low Noise, Linear Hall Effect Sensor ICs with Analog Output, A1324-DS, 2011.

[29] Texas Instruments, Infrared Thermopile Sensor in Chip-Scale Package, SBOS518A, May. 2011.

[30] F.W. Bell, Milwaukie, OR . http://fwbell.com/home.aspx.

[31] Texas Instruments, TMP006 Layout and Assembly Guidelines, SBOU108, May. 2011.

[32] Fluke Corporation, Everett, WA. http://www.fluke.com/.

[33] GF AgieCharmilles, Geneva, Switzerland. http://www.gfac.com/content/gfac/com/en.html.

[34] DuPont, DuPont Kapton HN Technical Datasheet ,K-15345-1, April 2011.

[35] Dassault Systmes SolidWorks, http://www.solidworks.com/.

[36] A. T. Zehnder and A. Ingraffea, "Reinforcing effect of coverlayers on the fatigue life of copper-kapton flex cables," *Components, Packaging, and Manufacturing Technology, Part B: Advanced Packaging, IEEE Transactions on*, vol. 18, no. 4, pp. 704–708, 1995.

[37] B. P. Ruddy, *High force density linear permanent magnet motors : "electromagnetic muscle actuators"*. PhD thesis, Massachusetts Institute of Technology. Dept. of Mechanical Engineering, 2012.

[38] A. Brown, "Modeling and characterization of a voice coil motor," 2012.

[39] O. A. Shergold, N. A. Fleck, and T. S. King, "The penetration of a soft solid by a liquid jet, with application to the administration of a needle-free injection," *Journal of biomechanics*, vol. 39, no. 14, pp. 2593–2602, 2006.

[40] COMSOL Multipysics, Burlington, MA. http://www.comsol.com/.

[41] Futek, www.futek.com.

[42] OMEGA Engineering, *OMEGA DLC101 Force Sensor Operator's Manual M1642/0493.*

[43] Henkel, Loctite 382 Techincal Data Sheet, Oct. 2008.

[44] W. Young and R. Budynas, *Roark's Formulas for Stress and Strain.* McGraw-Hill Companies, The, seventh ed., 2002.

[45] R. Williams, N. Hogan, P. M. F. Nielsen, I. Hunter, and A. Taberner, "A computational model of a controllable needle-free jet injector," in *Engineering in Medicine and Biology Society (EMBC), 2012 Annual International Conference of the IEEE*, pp. 2052–2055, 2012.

[46] Heidenhain,Schaumburg IL. `http://www.heidenhain.us/`.

[47] Renishaw, Gloucestershire, UK. `http://www.renishaw.com/`.

[48] MicroE Systems, Bedford, MA. `http://www.microesys.com/`.

[49] Advance Reproductions Corporation, North Andover, MA. `http://www.advancerepro.com/`.

[50] Denton Vacuum,Moorestown, NJ. `http://www.dentonvacuum.com/`.

[51] National Instruments LabVIEW, `www.ni.com/labview/`.

[52] C. Parsons, James S. (Laguna Niguel, "Needleless hypodermic jet injector," January 1998. US Patent 5704911.

[53] J. W. Bingham, "Vial system and method for needle-less injector," February 2007. US Patent 20070027428.

[54] C. U. Landau, Sergio (Laguna Niguel, "Needle-free injection device," April 2006. US Patent 20060089594.

[55] S. Lilley, J., D. R. Taylor, Hugh F. Theobald, C. J. Carlson, D. I. Rosen, and T. R. Johnson, "Medical injection system and method, gas spring thereof and launching device using gas spring," February 1997. US Patent 5599302.

[56] Bayer Material Science, Pittsburgh, PA, *Snap-Fit Joints for Plastics: a design guide.*

[57] 3D Systems Corporation, Accura 60 Plastic, PN 70712 , April 2008.

[58] R. Janssen, *Elastomeric closures for parenterals*, ch. 13, pp. 324–357.

[59] W. Curry, S. Conway, C. Goodfield, K. Miller, R. Mueller, and E. Polini, "Reducing the risk of contamination of sterile parenteral products via ready-to-use closure components," *AAPS PharmSciTech*, vol. 11, no. 4, pp. 1572–1579, 2010.

[60] Parker, *Parker O-Ring Handbook.* ORD 5700.

[61] W. J. Kudrowitz, Barry M; Fienup, "The exploration of concepts for projectile toys," Master's thesis, Massachusetts Institute of Technology. Dept. of Mechanical Engineering, 2006.

[62] A. Greenhut, "An analysis of buckling in spherical shells and its design implications for hopper poppers," Master's thesis, Massachusetts Institute of Technology. Dept. of Mechanical Engineering, 2006.

[63] S. Galiev, J. Blachut, E. Skurlatov, O. Panova, G. Moltschaniwskyj, and Z. Cui, "Experimental and theoretical design methodology of hemispherical shells under extreme static loading," *Strength of Materials*, vol. 36, no. 5, pp. 518–524, 2004.

[64] R. Zoelly, "Promotionarbeit," *Technische Hochschule*, 1915.

[65] Yurjevskij Universitet, *Proceedings of Tartu University*, 1917.

[66] H. J. Qi, K. Joyce, and M. C. Boyce, "Durometer hardness and the stress-strain behavior of elastomeric materials," *Rubber Chemistry and Technology*, vol. 76, pp. 419–435, May 2003.

[67] R. G. Mushtary, X. M.and Syrkin, "About nonlinear theory of buckling of elastic equilibrium of thin spherical shell under action of uniformly distributed normal external pressure," *Appl. Math. Mech*, vol. 14, p. 573586, 1950.

[68] A. Brinkmeyer, M. Santer, A. Pirrera, and P. Weaver, "Pseudo-bistable self-actuated domes for morphing applications," *International Journal of Solids and Structures*, vol. 49, no. 9, pp. 1077 – 1087, 2012.

[69] A. Brinkmeyer, A. Pirrera, M. Santer, and P. Weaver, "Pseudo-bistable pre-stressed morphing composite panels," *International Journal of Solids and Structures*, vol. 50, no. 78, pp. 1033 – 1043, 2013.

[70] M. Santer, "Self-actuated snap back of viscoelastic pulsing structures," *International Journal of Solids and Structures*, vol. 47, no. 24, pp. 3263 – 3271, 2010.

[71] G. A. Vliegenthart and G. Gompper, "Compression, crumpling and collapse of spherical shells and capsules," *New Journal of Physics*, vol. 13, no. 4, p. 045020, 2011.

[72] Smooth-On, PMC 121 Series, Sept. 2011.

[73] 3D Systems,Rock Hill, SC. `http://www.3dsystems.com/`.

[74] Henkel, Loctite 4014 Techincal Data Sheet, Feb. 2010.

[75] J. F. Kubiatowicz, "Popper toy," May 1979. US Patent 4152863.

[76] P. Staats and W. E., "Contrast delivery syringe with internal hydrophilic surface treatment for the prevention of bubble adhesion," November 2003. US Patent 6648860.